Discover Nano

Research

Tunable properties of silver (Ag) substituted $BaFe_2O_4$ nanoparticles for photovoltaic (PV) applications

Irum Shahid Khan[1] · **Iftikhar Hussain Gul**[1]

Received: 13 January 2025 / Accepted: 21 April 2025
Published online: 13 May 2025

Abstract
In this work, $Ba_{1-x}Ag_xFe_2O_4$ (x = 0.0, 0.2, 0.3, 0.5) nanoparticles have been prepared using the sol–gel auto-combustion method providing the pioneering investigation of substitution of silver into barium ferrite, that is often associated with magnetic applications. A broad inspection has been performed on structural, magneto-electric, dielectric, and optical properties uncovering potential of Ag incorporated barium ferrite nano particles using X-ray diffraction, Vibrating sample magnetometer, Multiferroic system, Impedance Analyzer, UV visible diffuse reflectance spectroscopy, Fluorescence spectrophotometer and Photoluminescence (PL) system. The chemical bonding and functional groups of all samples were explored by Fourier transform infrared spectrometer as well as with RAMAN spectroscopy. The slight turn in orthorhombic structure from (Pnma 62) to (Bb21m 36) was detected from pure $BaFe_2O_4$ particles to Ag concentrated samples and also illustrated in 3D visualization. The formation of spherical nanoparticles (46-32 nm) with designed composition ($Ba_{0.8}Ag_{0.2}Fe_2O_4$, $Ba_{0.7}Ag_{0.3}Fe_2O_4$, $Ba_{0.5}Ag_{0.5}Fe_2O_4$) which was confirmed by Scanning electron microscopy and Energy dispersive x-ray spectroscopy separately. The maximum magnetization value of 22.3 emu/g was revealed by the $Ba_{0.5}Ag_{0.5}Fe_2O_4$ sample. The lowest energy band gap value of 1.5–1.8 eV was achieved by pristine and $Ba_{0.7}Ag_{0.3}Fe_2O_4$ making it eligible to operate within the ideal region of solar cell efficiency with reduced recombination losses. The PL emission intensity was also observed in the visible spectrum at 573–576 nm for Ag concentrated samples suggesting that material can efficiently absorb and release light in the solar spectrum's most useful region. Significant leakage current was indicated by the PE loop with high conductivity, indicating that the material has reduced resistance and enhanced charge transport. Simulating solar illumination was used to evaluate the photovoltaic performance of nanoparticles, producing response curves for photocurrent and dark current revealing the improved photo current with Ag infusion. The valuable results of Ag-infused barium ferrites for dielectric, optical, and photovoltaic capabilities offered a fresh concept for using magnetic nanoparticles modified by silver as an encouraging development in the PV applications.

Keywords Alkaline earth metal Ba · Ferro-magnetic nanoparticles · Noble metal Ag · Orthorhombic ferrites · Sol–gel · Structural

✉ Irum Shahid Khan, ishahid.phdscme@student.nust.edu.pk; Iftikhar Hussain Gul, iftikhar.gul@scme.nust.edu.pk | [1]Thermal Transport Laboratory, Department of Materials Engineering, School of Chemical and Materials Engineering (SCME), National University of Sciences and Technology (NUST), Islamabad, Pakistan.

1 Introduction

Trends and the energy transition indicate that concerns over global warming, energy safety, and growing pollution in the air are leading to a greater emphasis in recent years on shifting from fossil fuels to energy from renewable sources. Numerous nations have set goals to increase the proportion of renewable energy in their energy stream, and since technological improvements, renewable energy is becoming more affordable than conventional sources. Solar cells and photovoltaic devices have grown significantly in recent years through their potential to capture the sun's clean, renewable energy. Such devices directly turn sunlight into power, providing an environmentally friendly alternative to conventional fossil fuels [1, 2] and emphasizing the necessity to switch to cleaner forms of energy revealing the importance of photovoltaic technology even more. The importance is based on the fact that photovoltaic technology generates electricity by utilizing sunshine, an infinite and renewable resource. Unlike fossil fuels, solar energy does not emit greenhouse gases or cause air pollution, making it an ecologically friendly energy source. The usage of photovoltaics considerably reduces the carbon footprint linked with power generation. Solar cells also subsidize qualifying environment change and reach the targets of reducing global emissions by shifting the need for power generation that is based on fossil fuel [3, 4]. Solar electricity can be used for a variety of purposes for its scalability and can be harvested in isolated locations where installing standard electricity infrastructure is challenging or expensive [5, 6].

Extensive research into innovative photovoltaic materials has been conducted in an effort to overcome the shortcomings of conventional solar cells, as a result of the pressing demand for efficient and sustainable energy sources. Numerous materials for photovoltaic solar cells based on nanoparticles have been discovered to improve efficiency and cost-effectiveness. Due to their size and make-up, nanoparticles have distinctive features that enhance light absorption, charge transport movement, and overall device efficiency [7, 8]. However, effectively incorporating nanoparticles into solar cell technology requires careful consideration of elements, including manufacturing scalability, compatibility, and stability [9–11]. The ability of a material to form pairs of electron-holes, which are necessary for the operation of a solar cell, and to absorb light depends critically on its band gap. The band gap of the typical photovoltaic material is between 1 and 1.8 eV [12].

An external electric field can inverse the spontaneous electric polarization that occurs in a type of material known as ferroelectric materials. The potential of ferroelectric photovoltaic (FPV) materials to produce energy through the photovoltaic effect, comparable to conventional solar cells, has been investigated. The creation of excitons employing light photons absorbed by a substance is known as the photovoltaic effect [13]. These electron–hole pairs can be separated in ferroelectric materials with spontaneous polarization, which generates photocurrent [14, 15]. Ferroelectric Materials are used in two ways commonly first by depositing thin films of materials on substrates, e.g. $(Pb_{0.97}La_{0.03})$ $(Zr_{0.52}Ti_{0.48})$ O_3 [16] $[KNbO_3]$1-x [BaNi ½ Nb ½ O_{3-}]x [17], $BiFeO_3$ [18] $BaTiO_3$ [19]. There are, however, just a few studies in this area that are pertinent to nanosized ferroelectric layers, including Si-doped HfO_2 [20], PLZT [21], $Pb(Zr_{20}Ti_{80})O_3$ decorated with nanoparticles of silver [22], Sb-doped AgO [23], $BiFeO_3$ [24–26] and $Bi_4Ti_3O_{12}$ [27].

Ferrites are a noteworthy family of materials that have long convinced industrial demand because of their various technical uses. These are categorized as ferromagnetic materials based on how the ferrite materials respond to a magnetic field, they are divided into two domains: soft and hard ferrites. However, if the structure of the ferrites is considered, it may further divide them into four categories. Garnet, spinel, magneto plumbite, and orthoferrites are the four groups. Each ferrite has a distinct role in the industry based on its structure and magnetic reaction. Hexaferrites and spinel have been extensively researched among ferrites because to their innovative and useful applications [28, 29]. The spinel ferrites represented by MFe_2O_4 are those in which M is readily substituted by various divalent ions or by combining any divalent ions such as Co, Cu, Ni, Mg, Mn, Zn. The spinel ferrite nanomaterials, which are used extensively in magnetic resonance imaging, photocatalysis, memory storage, drug targeted delivery, and other fields, are distinguished by their high saturation magnetization and electrical resistivity, low eddy current, and low cost. $CuFe_2O_4$, a member of the fascinating spinel ferrite group, is a material of great scientific interest and a highly sought-after material for a variety of technological applications of energy conversion and storage due to its wide range of remarkable physical properties, unique crystal structure, and appealing optical, electrical and magnetic properties [30]. $CoFe_2O_4$ has attracted the attention of numerous scientists from the search community because of its distinct structure-magneto-optic properties with addition of having a controllable optical band gap, high coercivity with low magnetization at normal temperature, great magnetic anisotropy in specific crystallographic [31, 32]. Similarly, many studies have been conducted on different spinel ferrites e.g. $ZnFe_2O_4$ [33–35] for improved effectiveness and examining cytotoxicity in cancer, electrode material in supercapacitors, biomedical applications, $CaFe_2O_4$ [36, 37] for

electronic, biomedical, energy and spintronic applications, [38] $NiFe_2O_4$ $MnFe_2O_4$ and $MgFe_2O_4$ [38–42] for electric, magnetic, biocompatible, catalytic, human health, technology and electrochemical applications.

It is a well-renowned fact that by using a specific synthesis method and adding the right impurities, properties of spinel ferrites are adjusted. The primary benefit of adjusting the characteristics of these materials lies in their capacity to distribute the cations on various interstitial sites, specifically B and A sites, which are referred to as octahedral sites and tetrahedral accordingly [43, 44]. The particle size is an impressive aspect of their properties; when the particle size decreases, it changes to a single domain. Because of their unique uses in a variety of fields, from telecommunication to medicine, we were motivated by this reputation to look into the magnetic and structural characteristics of crucial spinels as well as the effects of incorporation of the noble metal and alkali earth elements on their structure.

Barium ferrite ($BaFe_2O_4$) has a comparatively narrow range of uses in photovoltaics. Regarding $BaFe_2O_4$'s optoelectronic characteristics and appropriateness for effective absorption of light and charge carrier transport in photovoltaic devices, there is a substantial research gap. However, due to their distinctive characteristics and prospective uses in various industries, such as electronics, magnetics, and catalysis, these nanoparticles have gained attention gradually. The composition of the dopant, the synthesis process, and the results of doped or substituted barium ferrite nanoparticles will determine the specific uses and outcomes. These nanoparticles have been produced through various synthesis techniques, each with unique features that may impact their prospective applications [45]. Here are several typical ways of making $BaFe_2O_4$ nanoparticles, their characteristics, and prospective uses such as the sol–gel method [46], hydrothermal method [47], co-precipitation method [48], solid-state thermal decomposition process [49] etc. These are important for capacitors and other electrical devices because they display high dielectric constants. Due to their adsorption and catalytic capabilities, these nanoparticles have been investigated for their potential in removing heavy metals and pollutants from water. The size of $BaFe_2O_4$ nanoparticles can impact how they behave. Smaller nanoparticles may exhibit improved magnetic behaviour and surface reactivity [50–52].

It is possible to modify the structural, optical, magnetic, and electrical characteristics of barium ferrite nanoparticles to make them better suited for photovoltaic (PV) applications. The material's optical properties can be changed by mixing different compounds or by doping it with different elements [53]. Doping, substitution and incorporation can impact carrier concentration, optical characteristics, and the band gap, which can control how well the material converts solar energy. The following are some possible dopant kinds: non-metal dopants, transition metal dopants [54], and rare earth dopants [55]; their effects are better light absorption, boosted charge separation and transportation, optimized band gap, enhanced stability, and permanency, empowering versatile and flexible solar cell design [56, 57].

$BaFe_2O_4$ is occasionally classified alongside magneto plumbite type ferrite because of their similar magnetic characteristics, which causes some misunderstanding. Their crystal structures, however, are essentially unlike. Many researchers are extensively studying hexa barium ferrites ($BaFe_{12}O_{19}$) because of their massive dc resistivity, immense magnetic characteristics, small dielectric, and eddy current loss [58] but focused on the mono type. The properties of silver (Ag) nanoparticles can be tailored and used to improve photovoltaic traits and possibly boost solar cell efficiency as per the literature study. Ag nanoparticles display localized surface plasmon resonance when incident light excites the metal's electrons. Increased photon absorption from plasmonic phenomena can boost cell efficiency [59]. Ag nanoparticles have a wide range of light-scattering capabilities. This scattering can lengthen the path that light takes inside the solar cell material, increasing the likelihood that photons will be absorbed and decreasing reflection losses at the cell's surface. The plasmonic characteristics of Ag nanoparticles lead to an improved local electromagnetic field surrounding the particles, triggering stronger light-matter interactions [60]. It improves photon absorption and higher production of excitons. It facilitates charge separation by speeding up the transport of electrons between the semiconductor material and the nanoparticles. This may lower recombination losses and increase the effectiveness of charge collection [61, 62]. Ag nanoparticles can affect the material's band gap and energy levels when appropriately incorporated into semiconductor materials. This may alter the material's absorption spectra and enable it to match a wider variety of solar wavelengths, leading to increased efficiency [63]. Typical indium tin oxide (ITO) substrates can be replaced with transparent conductive Ag nanoparticle electrodes, allowing more sunlight to reach the solar cell while maintaining good conductivity. Ag nanoparticle integration into photovoltaic technology holds promise, but obstacles must be solved, including nanoparticle rigidity, scalability, and cost-effectiveness [64]. Ag nanoparticles'dimensions, distribution, and concentration must be carefully considered to increase efficiency. Researchers are still investigating alternative approaches for incorporating them into solar cell configurations to take advantage of Ag nanoparticles'specific features for enhancing energy conversion efficiency. Some key applications of silver nanoparticles in photovoltaic technologies and electronics are OLED displays and touchscreens as transparent conductive oxides, back reflectors and antireflection coatings in solar cells, conductive ink makings for

Table 1 Amount of chemicals used for the preparation of pristine and silver-substituted barium ferrite nanoparticles

Chemicals	Amount for pristine NPs		Amount for silver substituted NPs	
	mol	gm	mol	gm
Iron nitrate	0.2	8.08	0.2	8.08
Barium nitrate	0.1	2.61	0.08	2.10
			0.07	1.82
			0.05	1.30
Silver nitrate	–		0.02	0.34
			0.03	0.50
			0.05	0.84
Citric acid	0.9	18.91	0.9	18.91
Ammonia	~ 30 ml		~ 40 ml	
Deionized water	100 ml (for each salt)		100 ml (for each salt)	

printable electronics like flexible displays, wearable sensors, and radio frequency identification antenna (RFID) tags, and circuit boards. Similarly, supercapacitors and batteries with electrode material [65–67].

Since Ag incorporated $BaFe_2O_4$ nanoparticles has not yet been thoroughly studied for photovoltaic applications, this work represented a major advancement in the development of effective and magnetic active photovoltaic materials that can help for the application. By adding more free carriers, decreasing resistance, and encouraging effective charge transport, Ag inclusion can improve electrical conductivity. By reducing electron–hole recombination losses, this raises PV efficiency overall.

The study explores the use of the chemical element silver having high electrical conductivity in a magnetic host matrix designed for efficient photovoltaic material, aiming to improve light absorption, electronic structure, and dynamics of charge carriers. Our goal in this work was to create silver-substituted barium mono ferrite, which is typically soft ferrite and categorized as perovskite with partial structure and sometimes cubic. The current work presents the synthesis of $BaFe_2O_4$ nanoparticles with silver (Ag) substitution using the sol–gel technique via auto combustion. These silver-incorporated nanoparticles were studied magnetically, optically, structurally, and electrically for PV applications. Several reports have described the structural, magnetic, and electrical properties of mixed silver ferrites with other combinations but to the greatest extent of our acquaintance, no research has been done on the impact of silver on the optical, magnetic, and electrical characteristics of $BaFe_2O_4$ nano ferrites. To investigate barium mono ferrite's potential as a modern ferro magnetic material appropriate for photovoltaic applications, this groundbreaking study integrates silver (Ag) addendum into $BaFe_2O_4$ particles. The results of this study may open the door to the creation of novel and effective new materials for solar energy conversion technology.

2 Materials and methods

2.1 Materials

Iron nitrate nonahydrate [$Fe(NO_3)_3 . 9H_2O$] with (Mol. W: 404.00 g/mol) of minimum 99.0% ACS reagent purchased by Sigma Aldrich, barium nitrate [$Ba(NO_3)_2 . 5H_2O$] with (Mol. W: 261.36 g/mol) of assay minimum 99.0% purchased by UNI-CHEMICAL REAGENTS, silver nitrate hexahydrate [$Ag(NO_3)_2 . 6H_2O$], with (Mol. W: 169.87) of 99.8–100.5% purchased by Sigma Aldrich and citric acid [$C_6H_8O_7$] monohydrate with (Mol. W: 210.14 g/mol) ACS, EMSURE purchased by MERCK were the foremost precursors for nanoparticle's formation. The pH was adjusted with MERCK's exceptionally pure (25%) ammonia (NH_3) solution. The following (Table 1) is the exact amount of chemicals utilized to obtain the precise scheme of the particles.

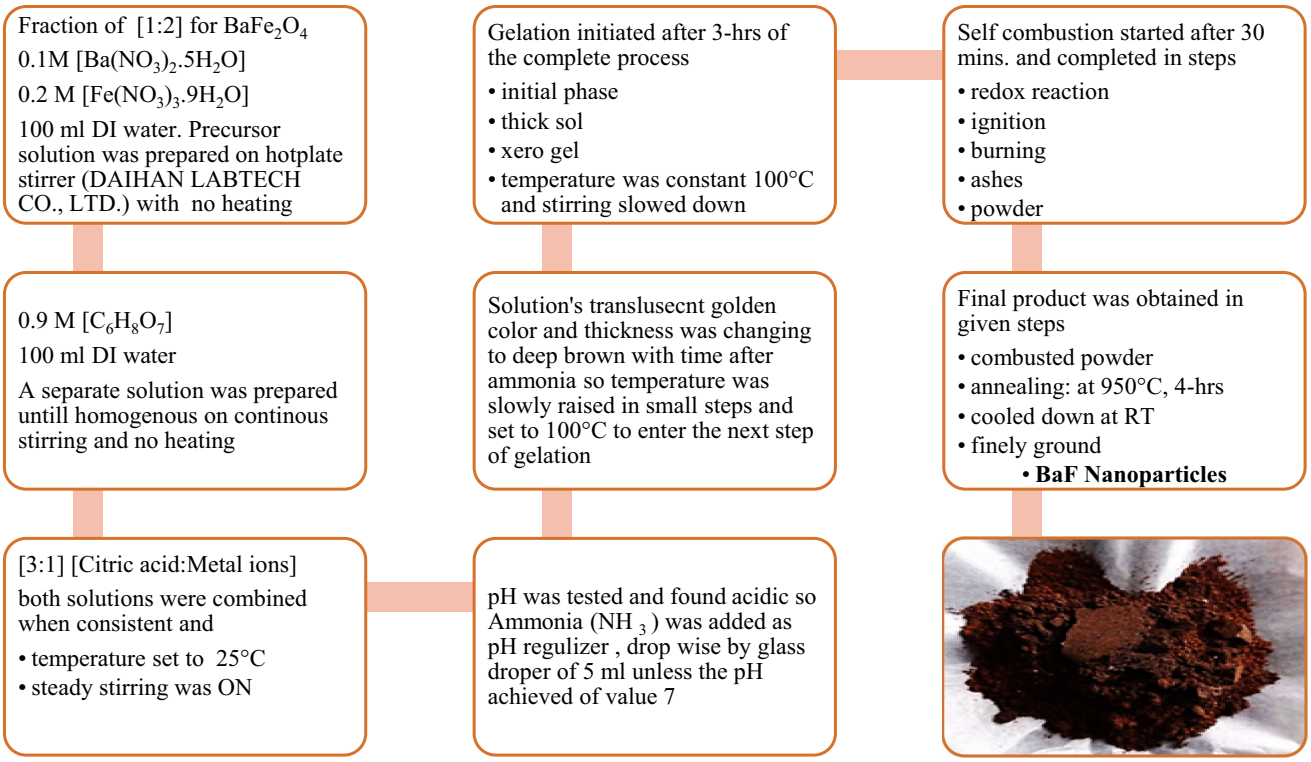

Scheme 1 Preparation process of pristine barium ferrite nanoparticles

2.2 Methods

2.2.1 Pristine barium ferrite NPs

$Ba_{1-x}Ag_xFe_2O_4$ nanoparticles were generated with a concentrations scheme of Ag (x = 0.0, x = 0.2, x = 0.3, and x = 0.5) by using the sol–gel auto combustion process. The synthesis process is fully demonstrated step-wise in scheme 1. To strengthen the crystal structure of pure barium ferrite, the resultant powder was ground in a mortar and pestle and then annealed in a muffle furnace (MAC5 A SHIMAX-1000 °C) for pristine barium ferrite nanoparticles.

2.2.2 Silver substituted barium ferrite NPs

The silver-substituted nanoparticles were prepared following the same scheme with the addition of silver nitrate solution in the precursors as presented in Fig. 1. There were many important factors e.g. fuel, pH, and selection of precursors taken care of the synthesis process in both cases that further affected the size, shape and properties of the prepared nanoparticles. Citric acid effectively delays any pre-precipitation by directing the metal ions. Because of its accessibility and affordability, it is the perfect fuel with metal ions to create nanoparticles in a balanced combustion environment. The citric acid was used in [3:1] to the metal solution in the synthesis. The type of metallic salts utilized in the synthesis decides this optimal ratio. Using a lower ratio frequently results in quick precipitation that produces little particles, while using a bigger ratio slows down development and reaction rates that produce huge particles. Additionally, because of this ratio, the fuel agent may balance heating throughout the combustion stage, converting the liquid into the required nanoparticle [68]. The pH of the solution was tested by the pH paper (pH 0–14 Universal Indicator SUPELCO) before and after the addition of ammonia. The acidic pH of the solution was balanced to a value of 7 which is considered neutral. The pH balance prevents extra precipitates from forming, which could alter the final powder's and gel's characteristics [69]. In the sol–gel process, it also influences the size and form of the particles; a value of 7 is ideal for the regulated morphology. For the first stages of hydrolysis and condensation, pH 7 also provides

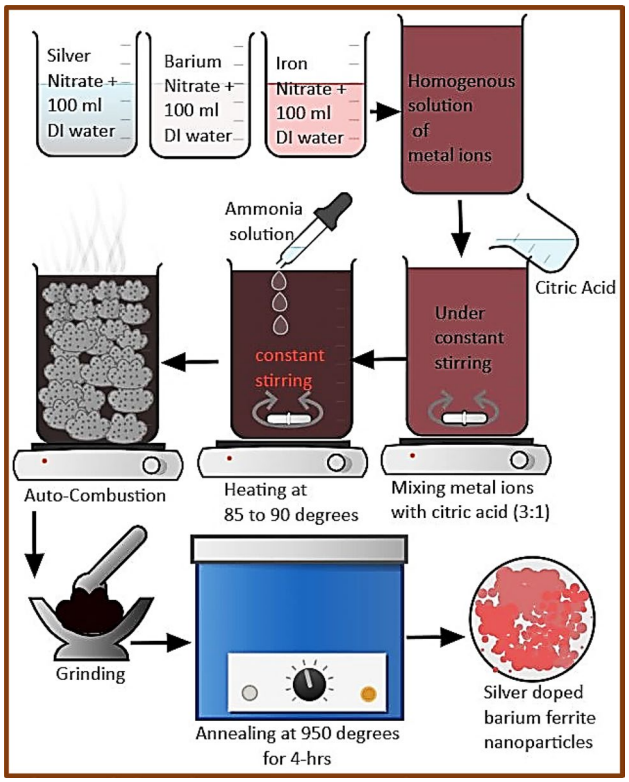

Fig. 1 Schematic of sol–gel process for the preparation of silver-substituted barium ferrite nanoparticles

a balanced environment. It is also thought to generate a regulated and effective combustion rate for the creation of the intended magnetic nanoparticles [70]. The temperature was raised to 90 °C after an hour of constant stirring while achieving the neutral pH of 7, and a rise in viscosity was seen. Since the transition between solution to gelation happens so quickly, it is challenging to detect precise viscosity when the solution begins to solidify as a result of shear thinning, hence viscosity testing is not a standard procedure in sol–gel. Although it is unavoidably a major factor influencing the end product, temperature, reaction kinetics, and precursor concentration can all be used to anticipate viscosity. Indirect indicators of viscosity include the solution's appearance as translucent, hazy, and thick, as well as the amount of time it takes for the solution to gel [71].

The reaction's subsequent step, auto combustion, involves the self-sustaining burning of metal nitrates and organic fuel in a gel precursor as shown in Fig. 1. Fire causes an exothermic redox reaction, which breaks down the gel quickly and produces metal oxide nanoparticles [72]. In this instance, the xerogel thickened after 25 min, and self-combustion continued for about 10 min unless all of the gel transformed to ashes that burned. After allowing the ashes to cool fully in the beaker, they were roughly crumbled in a mortar and pestle, yielding was measured. The powder was then annealed in a muffle furnace for four hours at 950 °C to enhance the silver-substituted barium ferrite nanoparticles'crystal structure. After finely grinding the annealed powder on the following day, the yield was once more measured and a decrease was seen. To prevent environmental moisture, the finished dark brown powder was marked and stored in a glass vial within the desiccator. The pure and silver substituted nanoparticle's potential chemical equation for the final product can be expressed as follows:

$$Ba(NO_3)_2.5H_2O + Fe(NO_3).9H_2O + C_6H_7O_8 + NH_3 + heat + CO_2 + H_2O + side\,products$$

$$Ba{-}C_6H_7O_8 + Fe{-}C_6H_7O_8 + Ag{-}C_6H_7O_8 + NH_3 \rightarrow Ba_1{-}_xAg_xFe_2O_4 + \text{co prods.} + H_2O + C.A_{derivative}$$

2.3 Techniques

An X-ray diffractometer (DRON-8 pXRD) analysis was performed to identify the structure of the acquired dark brown powder. The FTIR Spectrometer (Bruker Alpha) was used to determine the functional groups of the obtained powder. All

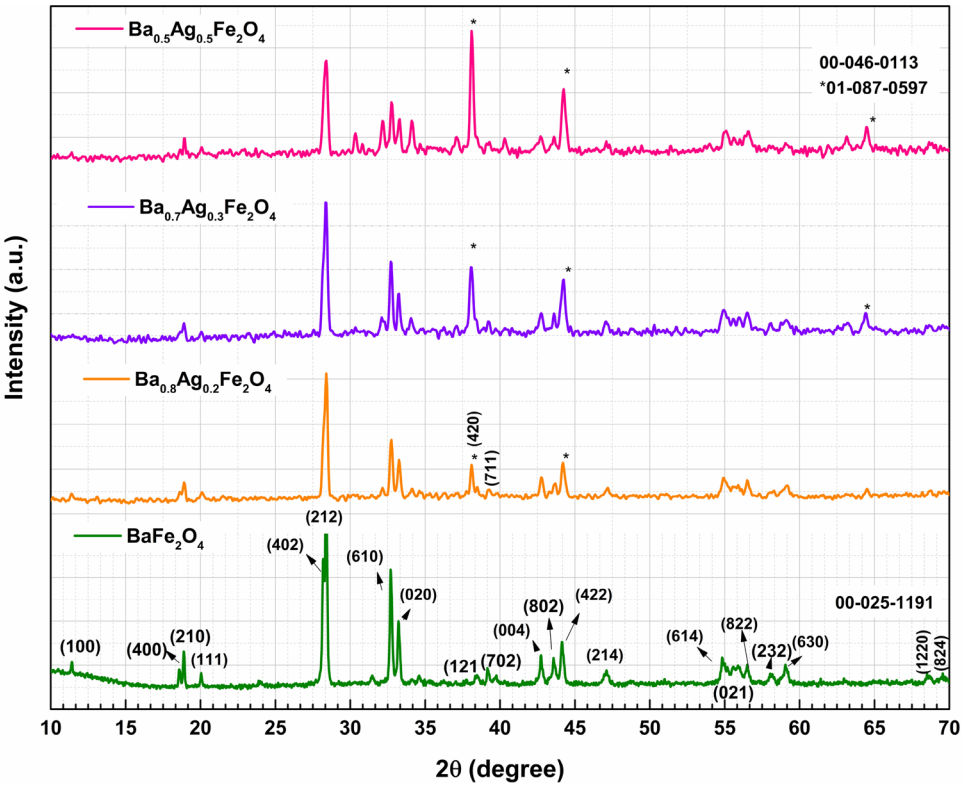

Fig. 2 X-ray diffraction patterns of the barium ferrite nanoparticles and with silver substitution

of the powder samples were also gone through RAMAN Spectroscopy for compositional bonds by BWS415-532S-iRaman (Newark, NJ, USA). The suspension of the resulting powder in deionized water enabled surface morphology analysis using an SEM (JEOL-instrument JSM-6490 A) equipped with Energy dispersive x-ray spectroscopy EDS, and later grain size was measured by ImageJ software. The nanoparticle's powder weight of 0.05 gm of each sample was also inspected separately for magnetic performance using VSM (NEWTECH PRO II X9). The disc pellets were formed using a pressure of 100 psi for 8 to 10 min and later annealed at 900 °C for 1 h for dielectric investigation utilizing Impedance Analyzer (WAYNE KERR 6500B). The disc pellets had a powder weight of 0.462 gm, a diameter of ~ 13 mm, and a 2.00–2.31 mm thickness. The optical characteristics of powder samples were investigated using a UV–visible diffuse reflectance (DRS) spectrophotometer and later followed by a fluorescence spectrophotometer (Perkin-Elmer FL 6500). A multiferroic system (RADIANT TECHNOLOGIES INC.) was used to evaluate the ferroelectric manners. The photoluminescence spectra were recorded by HORIBA Scientific SampleMax sample compartment facilitated with HORIBA'S MicroHR spectrometer. The photovoltaic behaviour was recorded by NEWPORT Oriel Sol3 A solar simulators (AM 1.5G filter standard) with 1 SUN output power.

3 Results and discussion

3.1 Structural and surface analysis

3.1.1 X-ray diffraction (XRD)

Figure 2 reveals the patterns of silver substituted and pure barium ferrite nanoparticles'crystal structures attained at 950 °C temperature by annealing for 4 h. The XRD scattering was performed by Cu K-alpha radiation of 1.5406 Å wavelength in a 2-theta angle range of 10 to 80°. The XRD pattern exposed orthorhombic structure having a single phase with Pnma E space group no. 62 for pristine $BaFe_2O_4$ particles. The noticeable peaks patterned were (210), (111), (402), (212), (610), (020), (004), (802), (422), (214), (614), (822) and (630) at 2-theta position of 18.8°, 20.0°, 28.1°, 28.4°, 32.7°, 33.2°, 42.6°, 43.5°, 44.1°, 54.8°, 56.5°, 58.0° and 59.0° for pure $BaFe_2O_4$ crystal planes that entirely matched one to one to the JCPDS No. 00–025-1191 and confirmed the formation of orthorhombic structure.

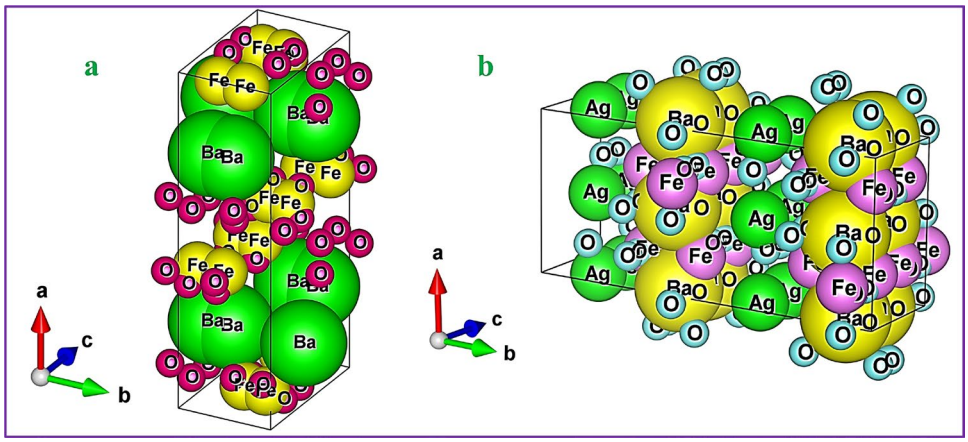

Fig. 3: 3D atomic radii visualization of transition of orthorhombic crystal structure from **a** Pmna-62 to **b** $Bb2_1m$-36 for pure barium ferrite to Ag = 0.5 substituted nanoparticles

Table 2 Calculated lattice parameters of barium ferrite nanoparticles with silver substitution

Lattice Constants (Å)	Standard Values JCPDS 025–1191	Standard Values JCPDS 046–0113	Calculated Values			
			$BaFe_2O_4$	$Ba_{0.8}Ag_{0.2}Fe_2O_4$	$Ba_{0.7}Ag_{0.3}Fe_2O_4$	$Ba_{0.5}Ag_{0.5}Fe_2O_4$
a	19.05	19.04	19.26	19.38	18.95	19.0
b	5.39	5.38	5.47	5.30	5.38	5.39
c	8.45	8.44	8.45	8.31	8.47	8.5
Standard Volume (10^6 pm^3)	867.44	865.72	877.37	853.55	863.52	870.48
Standard density (g/cm^3)	4.79	4.80	4.74	4.77	4.67	4.55

The other peaks were found at 2θ = 37°, 38.2°, 44.3°, 64.5° and 77.3° displaying the presence of Ag in samples for x = 0.2 to 0.5 and matched to JCPDS No. 01–087-0597 (Ag) for Ag substitution. The changing phase with the substitution of silver was detected by a single peak (212) that appeared as a single merging peak of (212) and (402) in substituted samples. However, the orthorhombic crystal structure was the same maintained with Ag concentrations of x = 0.2 and 0.3, but the group was shifted from Pnma 62 to $Bb2_1m$ 36 with a slight difference in the sample where x = 0.5 as per JCPDS score of 00–0046-0113. The potential configuration of Ba, Fe, and O on the atomic sites supplied as JCPDS 00–025-1191 of orthorhombic (Pnma-62) and $Bb2_1m$-36 was illustrated in 3D by VESTA software in Fig. 3a, b to enhance comprehension arrangement of pure $BaFe_2O_4$ and $Ba_{0.5}Ag_{0.5}Fe_2O_4$. To the best of our knowledge, Fig. 3 is our attempt to provide a potential concept for the atomic organization for pristine since the crystallographic database file for the precise crystal arrangement and exact space group pairing for $BaFe_2O_4$ was not available. Ba^{2+} typically occupies bigger, more open places in the structural phase (Pnma-62) of the orthorhombic system, and the sites are octahedral rather than tetrahedral. Ba^{2+} ions are found in larger coordination positions because of their large ionic radius (1.34 Å). Since Fe^{3+} has an ionic radius of 0.64 Å, which is significantly less than that of barium, it will also be seen in octahedral. O^{2-} typically occupies tetrahedral or octahedral positions, depending on the coordination number. It is positioned to balance the coordination and charge conditions of the surrounding cations [73]. In Pnma, tetrahedral sites are frequently smaller and less suitable for larger ions [36] (Fig. 3a).

Figure 3b displays the $Ba_{0.5}Ag_{0.5}Fe_2O_4$ crystalline structure for the $Bb2_1m$-36 arrangement. The ionic radius of silver is 1.26 Å so it covers the sites of barium ions at 4a. There are two types of barium atoms, with one ringing by seven atoms of oxygen and the other by eleven, with the distance between Ba^{2+} and O^{2-} ranging from 2.62 to 2.94 Å. Each Fe^{3+} atom is enclosed by tetrahedral surroundings made possible by four oxygen atoms [74]. Because Ba ions are relatively big, they most likely fill large ionic sites, perhaps at higher-symmetry Wyckoff locations and Ag interacts with nearby oxygen atoms when positioned interstitially, maybe at lower-symmetry locations. Fe^{3+} may interact with oxygen to fill octahedral or tetrahedral coordination. With the other atoms, O^{2-} forms a conventional framework around the metal cations [75].

The peak positions for the host and substituted samples were nearly identical, with only a slight variation in the whole width half maximum values indicating that Ag ions occupied sites of Ba at similar sites [76, 77]. The orthorhombic crystal

Table 3 Calculated structural parameters and crystallite size by Sherrer's formula of barium ferrite nanoparticles with silver increasing concentration

Samples	Average FWHM (rad.)	Average Micro-strain ($\varepsilon x10^{-3}$)	Average Dislocation Density ($\delta x10^{-3}$) (nm^{-2})	Average Crystallize Size D (nm)
$BaFe_2O_4$	0.0039	0.369	0.942	43
$Ba_{0.8}Ag_{0.2}Fe_2O_4$	0.0035	0.370	1.475	40
$Ba_{0.7}Ag_{0.3}Fe_2O_4$	0.0061	0.396	1.431	35
$Ba_{0.5}Ag_{0.5}Fe_2O_4$	0.0056	0.317	1.205	38

structure was used to obtain the lattice constants for the $BaFe_2O_4$ and Ag substitute samples presented in Table 2. Using Bragg's Law [78, 79] as given below, the value of interplanar spacing'd'was computed as follows:

$$n\lambda = 2dsin\theta \tag{1}$$

$$d = \frac{n\lambda}{2sin\theta}. \tag{2}$$

Here, the incident λ is the x-ray's wavelength, 1.5406, n is the order of diffraction, and the peak position θ in radians are all present. The computed values of various parameters [80, 81] like orthorhombic unit cell volume, lattice constants, and the x-ray densities of pure and Ag-incorporated nanoparticles, are detailed in Table 2. The relation for the orthorhombic crystal system is given as follows:

$$\frac{1}{d^2} = \frac{h^2}{a^2} + \frac{k^2}{b^2} + \frac{L^2}{c^2} \tag{3}$$

It was found that the sample $Ba_{0.7}Ag_{0.3}Fe_2O_4$ and pure $BaFe_2O_4$ both closely matched the standard lattice constant, volume, and density values of JCPDS 00–025-1191 and 00–046-0113. The constants"b"and"c"values were the same for all samples. The lattice constant values, volume, and density were slightly different in $Ba_{0.5}Ag_{0.5}Fe_2O_4$ but closer for $Ba_{0.8}Ag_{0.2}Fe_2O_4$ and $Ba_{0.7}Ag_{0.3}Fe_2O_4$.

The substitution ions were proven to make changes in host structure by this. The average crystal size of all nanoparticles was determined by the Debye–Scherrer formula [82], which is as follows:

$$D = \frac{0.9\lambda}{\beta \cos \theta} \tag{4}$$

D is the crystalline size in (nm), K is the Scherrer constant, and FWHM is radians.

Table 2 depicts various crystallographic parameters that show the structural characteristics of the produced nanoparticles. The rise in Ag concentration in the unadulterated $BaFe_2O_4$ nanoparticles decreased the average particle size between 43 and 35 nm. This crystallite size likewise approved the nano range of obtained particles. This change in size may be caused by the Ba^{+2} having a greater ionic radius (r) of 135 r(pm) compared to the Ag^{+2} 115 r(pm) [83].

The improvement that occurs with increasing Ag concentration is shown in Table 3 due to the computation of additional parameters, full-width half maximum, micro strain, and the density of dislocations [84] of the structure. Since the dislocation density and crystallite size have opposite relationships, a rise in dislocation density with increasing Ag concentration may have resulted from a reduction in the size of the crystallite of nanoparticles. The sample with Ag = 0.2 has the highest density and Ag = 0.3 has the smallest crystallite size. This computed shift in values also showed that the deformation in the lattice caused by the concentration of Ag got worse with further increasing concentration. As a result, a bond arrangement that increases internal pressure to compress lattice parameters and decrease crystallite size is absent. As shown in Table 3, this increase in micro strain was caused by the reduction in particle size [85]. The more insightful information about the size of crystallites, strain and peaks broadening was also explored by using Williamson Hall plots for all the samples using the relations:

$$\beta_T cos\theta = \epsilon(4sin\theta) + \frac{K\lambda}{D} \tag{5}$$

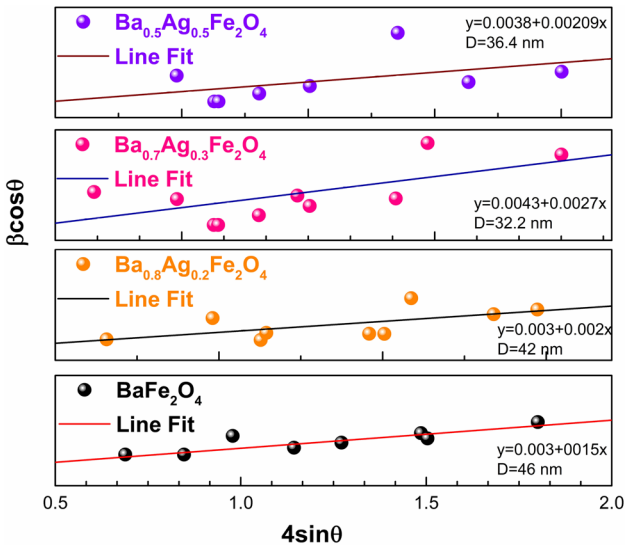

Fig. 4 The WH plots with y-intercept and linear fit slope for barium ferrite and silver substituted nanoparticles

where left side of the Eq. (5) represents the y-intercept that is taken on y-axis and the first part on the right side of the equation $4sin\theta$ is drawn on the x-axis of the WH plot. The 'ϵ' represents directly to the strain present and the part $\frac{K\lambda}{D}$ is used to calculate the crystallite size 'D' in nm. The relation (4) is compared to the straight-line equation $y = mx + c$ for the parameters. Figure 4 displayed the WH plots drawn likewise method by using a Gaussian fitting model on the XRD data, β_T, or FWHM, or total broadening owing to crystallite size and lattice strain, which was computed in radians. K is the form factor, which was 0.9. The X-ray wavelength is $\Lambda = 0.15406$ nm.

The above data (Table 4) showed that crystallite size gradually decreased from 46 nm as Ag substitution increases up to 0.3 Ag content, then slightly increases at the greatest content of Ag = 0.5. Lattice deformities and strain-induced suppression of grain growth caused by Ag inclusion, which interfered with the long-range crystal periodicity, are responsible for this drop. A slight improvement in crystallite size (36 nm) at the largest Ag concentration, however, raises the possibility of strain reduction mechanisms or the coalescence of small crystallites. At the same time, Ag substitution caused the lattice strain (ε) to increase, peaking at 0.3 Ag concentration ($2.7 \times 10^{-}3$). Increased defect density and lattice spin were indicated by the increase in strain, which might be brought on by the substitution of Ag ions into the $BaFe_2O_4$ lattice. Nevertheless, strain somewhat lowers at the maximum Ag = 0.5, most likely as a result of structural modifications that better accommodate the dopant and cause partial strain relaxation. However, variations in the particle size obtained using the W–H and Sherer approaches were noted due to underlying assumptions and mathematical formulations. The crystallite size, as determined by the W–H plot, is often greater than the value derived from the Scherrer equation [86]. The reason for this disparity is that whereas the W–H figure considers both size and strain contributions to peak broadening, the Scherrer equation only takes size into account. By separating the effects of strain and crystallite size, the W–H plot enables a more thorough understanding of the material's characteristics. However, the Scherrer formula fails to differentiate between strain and size, which may result in an oversimplified interpretation of the material's microstructure. These methods show how, in the field of materials research, microstrain, crystallite size, and element inclusion interact intricately.

3.1.2 Scanning electron microscopy (SEM)

Figure 5a–d left column shows SEM micrographs of spherical-shaped pure and Ag-substituted barium ferrite nanoparticles. Micrographs were taken from X50, 000 to X80, 000 magnification to study surface morphology, and the Image J program was used to determine the distribution and size of the particles. The outcomes following the completion of Image J's processing for each micrograph are shown in the right column of Fig. 5a–d. Some aspects that affect the final quantitative results'quality are a high-resolution image and a thorough comprehension of the sources of measurement uncertainties. The image was binarized following the correction of the file entered into Image J, which involves recalibrating the pixel size initially obtained with the SEM micrographs. It can be seen from Fig. 5 from a to d (right column) a

Table 4 Crystallographic parameters calculated by Willaimson Hall methods

Samples	Williamson Hall Calculation	
	Average Crystallite size (nm)	Average Microstrain (10^{-3})
$BaFe_2O_4$	46	1.5
$Ba_{0.8}Ag_{0.2}Fe_2O_4$	42	2.0
$Ba_{0.7}Ag_{0.3}Fe_2O_4$	32	2.7
$Ba_{0.5}Ag_{0.5}Fe_2O_4$	36	2.1

decrease in the width of columns of the histogram can be observed with reducing particle size. The particle size of pure barium ferrite nanoparticles 229 nm decreases with silver addition (22.0 nm, 60.7 nm, and 39.8 nm), satisfying the XRD results also. The minimum value in the contrasting histogram corresponding to the associated image must be adjusted appropriately to define the particle boundaries as precisely as feasible. The next essential step was to separate or exclude the agglomerated particles in sample Ag = 0.3 when the binarized and calibrated images are produced, and particle size is bigger than 0.2 and 0.5 samples. The agglomerated NPs were manually eliminated from the image due to their decreased quantity. Because of the light-saturated effect at the NPs'boundary caused by the in-lens detector's great sensitivity to sample interface electrical charge, there is a notable exaggeration of the NP size [87].

Ag and Ba have different ionic radii, and grain size is considerably reduced; Ag concentration rises in $BaFe_2O_4$ nanoparticles [88, 89]. Along with increased Ag concentration, grain distribution also declined. The Kirkendall effect also clarified that the variations might reduce the grain size of the host compound particle in diffusing rates between pure and incorporated elements [90, 91]. There were no signs of a porous structure or highly developed porosity on the particles' generally smooth surface. This finding was consistent with the ferrite nanoparticles'overall shape, which is typically non-porous or exhibits modest porosity. The ferrite nanoparticle synthesis method is also one of the elements that might influence porosity, and the sol–gel process frequently produces non-porous nanoparticles, as seen in this instance [92].

3.1.3 Energy dispersive X-ray analysis (EDX)

The activation of the EDS x-ray spectrometer, a feature found in the most advanced using energy-dispersive X-ray analysis to evaluate the nanoparticle's compositional elements as presented in Fig. 6 (a-d). According to Kim et al. [93], the separated nanoparticles are placed on an appropriate substrate that does not obstruct the nanoparticles'ability to be characterized. With a traditional SEM/EDX system, the possibility of a qualitative analysis by EDX and detecting each of the nanoparticles is quite low. For many years, a 10 mm^2 active regions EDX detector has been used. However, the componential EDX maps of nanoparticles can be successfully produced with conventional EDS detectors when the SEM's transmission mode is considered to significantly reduce the contribution of the traditional large substrate [94]. Figure 6 displays EDX maps of each sample, including silver substituted and barium mono-ferrite nanoparticles. SEM/EDX produced data regarding a sample's composition, including the elements present and their concentration and distribution. All the elements, such as Iron (Fe), Silver (Ag), Barium (Ba), and oxygen (O), were discovered. All the above components and Ag distribution were found in the utilized adsorbent analysis, indicating a uniform distribution of active adsorption sites. Together with the compositional maps, the EDS's computed weight percentage and atomic percentage are also tabulated in Table 4. The EDX results in Fig. 6 (a-d) demonstrated that no contaminants were discovered in the composition. The synthesized barium ferrite's stoichiometric ratio closely resembled the EDX values. It also confirmed that the synthesis's stoichiometry matches the measured quantity of each precursor used [95].

A glass substrate composed of Na, Si, Al, or Ca was used to test the particles. Later, the substrate was coated with gold (Au) to make it conductive. These distinctive peaks in the 1.5–2.5 keV range were typically seen in the EDS spectra and were left unidentified since labelling alters the intensity percentage of the primary elements [96]. The 4.5–5.6 keV range's unlabeled peaks are also for Ba. Typically, the silver (Ag) peaks are seen between 0.2, 2.6, and 3.0 keV [97, 98] as depicted in Fig. 6. Theoretical weight percentage and atomic percentage were computed using the following relations to verify the production of specimens of the proposed scheme:

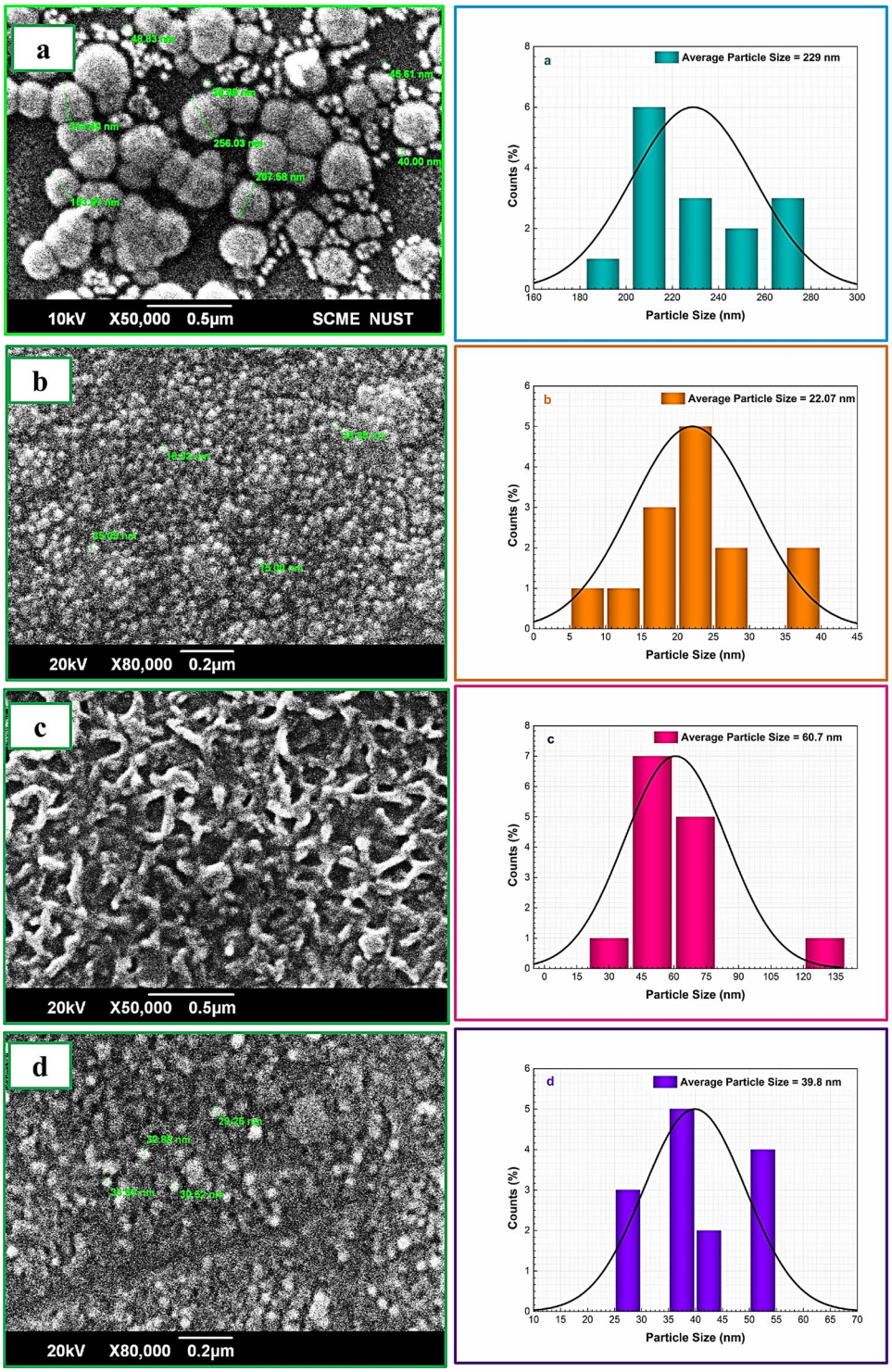

Fig. 5 SEM micrographs **a** $BaFe_2O_4$ **b** 0.2 Ag-substituted **c** 0.3 Ag-substituted **d** 0.5 Ag-substituted (left-column) with Measured Grain size and distribution of nanoparticles (**a**) $BaFe_2O_4$ (**b**) 0.2 Ag-substituted (**c**) 0.3 Ag-substituted (**d**) 0.5 Ag-substituted (right-column)

$$Each\ element\ weight\% = \frac{mass\ of\ each\ element\ in\ formula}{molar\ mass\ of\ the\ compound} \times 100 \tag{6}$$

$$Each\ element\ atomic\% = \frac{each\ element\ no\ of\ atoms\ in\ formula}{total\ no.\ of\ atoms\ of\ formula} \times 100 \tag{7}$$

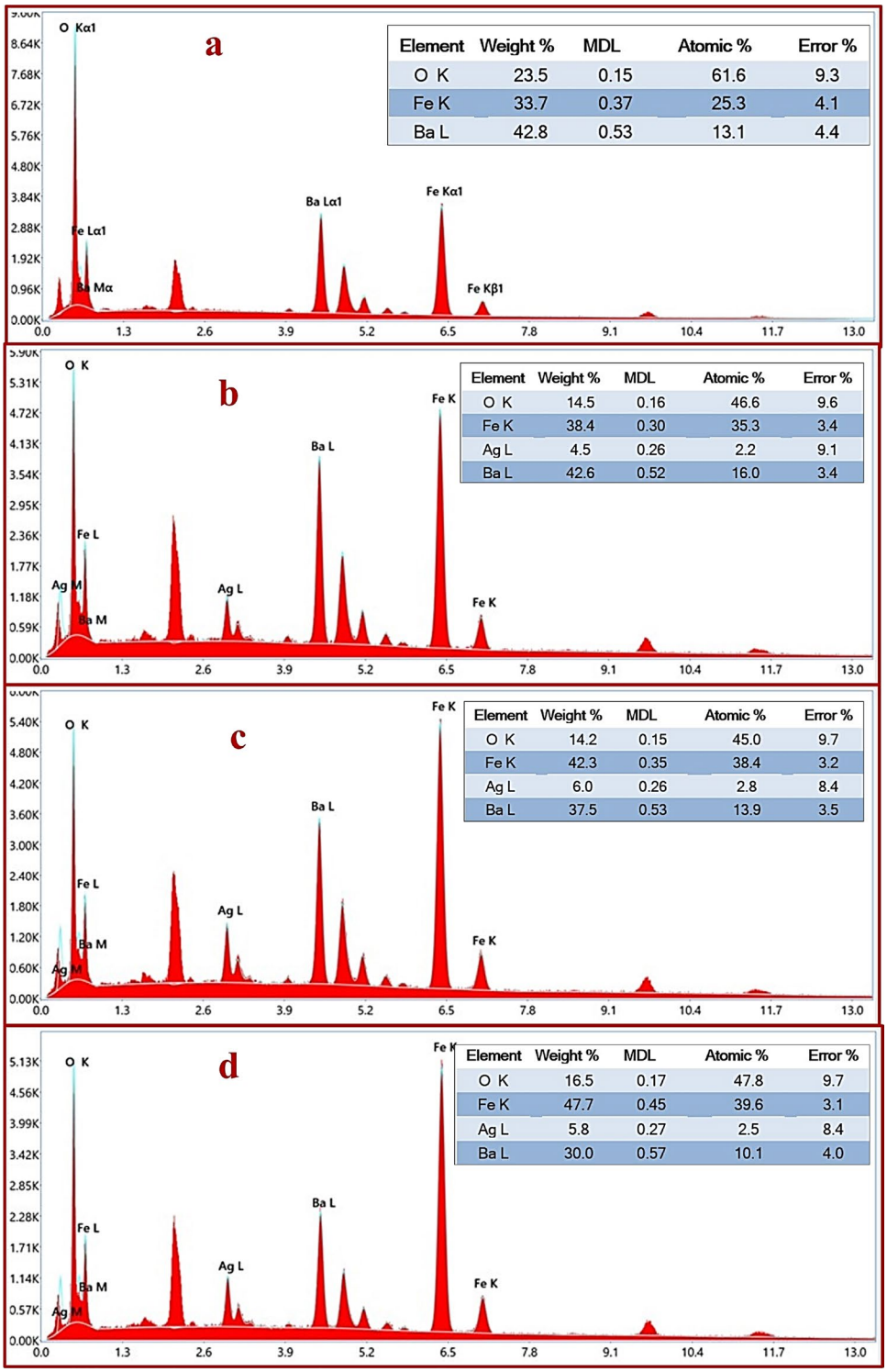

Fig. 6 EDS composition with identified elements and weight % **a** barium ferrite nanoparticles **b** 0.2 Ag-substituted **c** 0.3 Ag-substituted **d** 0.5 Ag-substituted

These calculated values for each element were tabularized in Table 5 after being compared to the data provided by EDS.

The intended compositions of the pure and Ag-substituted nanoparticles were confirmed by a close match between the presumed weight and atomic proportions of each element—Ag, Ba, Fe, and O—and the EDS data according to the sample's scheme. The consistency of the EDS data shows that the Ag concentration has increased in both weight and atomic ratios. This uniformity shows that the creation of the targeted nanoparticles is at the appropriate level, reflecting the elemental ratios required for optimal photovoltaic application. The precision of

Table 5 Comparison of theoretical and EDS values of compositional elements for pristine and silver-substituted NPs

Sample	Elements	Theoretical Data		EDS Data	
		Weight %	Atomic %	Weight %	Atomic %
$BaFe_2O_4$	Ba	43.9	14.3	42.8	13.1
	Fe	35.7	28.6	33.7	25.3
	O	20.4	57.1	23.5	61.6
$Ba_{0.8}Ag_{0.2}Fe_2O_4$	Ba	35.9	11.4	42.6	16.0
	Fe	36.4	28.6	38.4	35.3
	O	20.7	57.1	14.5	46.6
	Ag	7.0	2.9	4.5	2.2
$Ba_{0.7}Ag_{0.3}Fe_2O_4$	Ba	31.9	10.0	37.5	13.9
	Fe	36.7	28.6	42.3	38.4
	O	21.0	57.1	14.2	45.0
	Ag	10.7	4.3	6.0	2.8
$Ba_{0.5}Ag_{0.5}Fe_2O_4$	Ba	23.0	7.1	30.0	10.1
	Fe	37.4	28.6	47.7	39.6
	O	21.5	57.1	16.5	47.8
	Ag	18.1	7.1	5.8	2.5

the nanoparticle composition is strengthened by this alignment of the two data, which also validates the effectiveness of the synthesis process and the SEM/EDS configuration [99]. This relationship is significant because it demonstrates that to enhance the parent nanoparticles'characteristics for the intended use, the included silver should be distributed correctly in the nanoparticles. Additionally, this accuracy is necessary to maximize the electrical, magnetic, optical and photovoltaic features to improve the functionality of the silver-incorporated barium ferrite nanoparticles [100].

The acknowledged limits of EDS in identifying heavier substances like Ba and Ag, which are affected by X-ray absorption effects, were the cause of the observed differences in elemental percentages. The process of normalization affected and the semi-quantitative character of EDS analysis were blamed for the overestimation of Fe and O. The dependability of our synthesis was supported by XRD and SEM, which verified phase clarity without secondary phases in spite of these variances. Our composition also stayed within the anticipated range because our results were consistent with published literature.

3.2 Vibrational and RAMAN studies

3.2.1 Fourier transform infrared spectroscopy (FTIR)

Pure and Ag-substituted samples have been examined using FTIR to identify the presence and movement of chemical bonds. The IR spectra's 4000–400 cm^{-1} range (Fig. 7) was measured, although the peaks were only visible after 500 cm^{-1}. According to the findings in Fig. 7, the initial pair of peaks at 470, 497, 622 and 773 cm^{-1} with minor shifting from pristine to Ag concentrated sample represent vibrational stretching brought on by metals $Fe^{3+}O^{-2}$ and $Ba^{2+}O^{-2}$ in octahedral and tetrahedral sites, respectively [101]. In ferrites, bands at low frequencies (450 cm^{-1}) were linked to the vibration stretching of oxide of metal bonds at octahedral sites. In contrast, bands at high frequencies (500–630 cm^{-1}) were associated with tetrahedral sites [102, 103]. For such kind lattice vibration beneath 1000 cm^{-1}, the oxygen ions produced the bands in opposition to the metal ions. The formation of barium ferrite with an orthorhombic structure and the peak at 765.96 cm^{-1} were confirmed (Ba–O) [104, 105]. The following peaks (1095.0, and 1117.7 cm^{-1}) that shift slightly in the range 800 to 1200 cm^{-1} are associated with Ba^{2+}, Fe^{3+} and Ag^{+2}, metal–oxygen-metal manner of fingerprint, which is consistent with the prepared crystalline orthorhombic in the structure of MFe_2O_4 nanoparticles [106]. The next set of peaks in each sample shows the absorption of nitrate ions and corresponds to vibrations of bending at 1423–1438 cm^{-1} [107]. Peaks at 1627–1632 cm^{-1} and widespread absorption at 3418–3428 cm^{-1} were caused by the bending and stretched vibrations generated by the -OH bond for collected water and other hydroxyl function groups adsorbed on the nanoparticle surface [108, 109]. The remaining

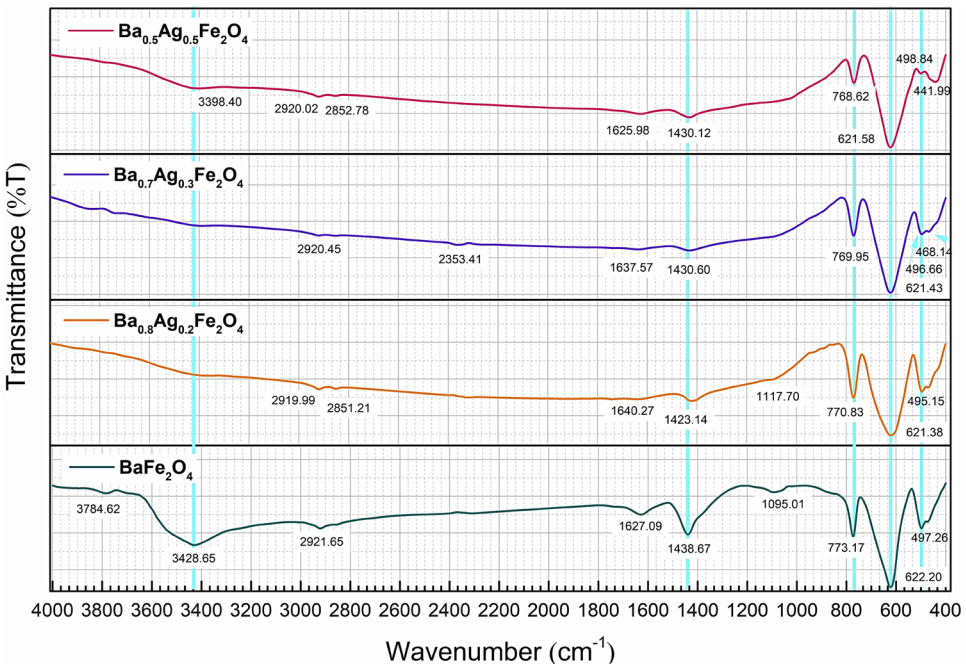

Fig. 7 FTIR spectrogram of barium ferrite nanoparticles with silver concentration

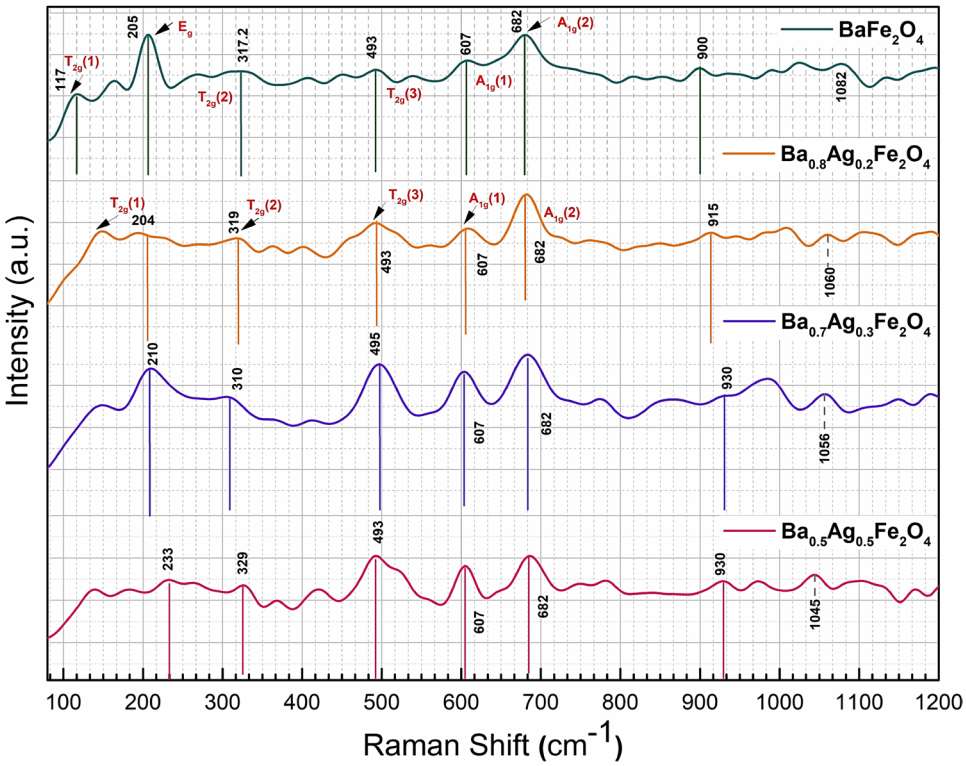

Fig. 8 Raman spectrum of barium ferrite nanoparticles with silver concentration

little peaks in the 2300–2950 cm^{-1} range can be attributed to the CO_2 absorption from surrounding air and the C–O vibrational stretching mode of the acetyl group found in the Ag specimens [110, 111].

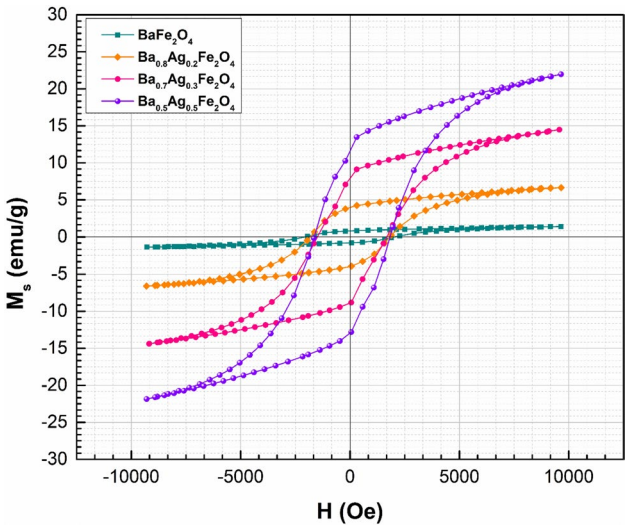

Fig. 9 Increasing saturation magnetization of barium ferrite nanoparticles and silver-substituted ones

3.2.2 Raman spectroscopy

Valuable information can be swiftly and readily obtained by Raman analysis (Fig. 8). It can be applied to quickly define any sample's structure and chemical form, solid, slurry, or powder. It is possible to predict the cation order in ferrite oxides, which permits additional structural connections that influence the magnetic behaviour of the infused or substituted ferrite nanoparticles [112].

According to the author's review of the literature, only a few studies are using Raman spectroscopy for a single phase of $BaFe_2O_4$, which means that the factor analysis of groups from the Bilbao crystallographic server [113] is the only source from which an estimation of all Raman-active vibrational modes can be made. $BaFe_2O_4$ usually has 16 Fe ions, 8 Ba ions, and 32 O ions in its unit cell of orthorhombic structure. The 16 Fe ions are located at crystallographic site 8b but are displaced from the typical structure at distinct positions [105]. It is estimated that 12 combinations of raman active vibration modes at the Γ point denoting the brillouin zone center and Γ equals $3B_1 + 3B_2 + 3\ A_1 + 3\ A_2$. Three stages of the transition phase can be identified by examining the outcomes of the Raman spectrum in the 110 cm^{-1} to 1200 cm^{-1} range in Fig. 8. All the raman peaks are seen in the first transition step under the findings of the phase identification using XRD [114]. The scheme of $Ba_{1-x}Ag_xFe_2O_4$ in Fig. 8 originated from the first step, where every vibrational mode resembles the $BaFe_2O_4$ raman active modes. Several prominent Raman peaks can be observed in substituted and pure samples at positions 205, 493 and 607 cm^{-1}, 117, 205, 210, 319, 329, 683, 900, and 1082, 1060. 1056 and 1045 cm^{-1}. These peaks are linked to the fingerprint position of the $BaFe_2O_4$ phase. Even though numerous Raman peaks at positions 204, 233, 209, 915, 930, 1060, 1056 and 1045 cm^{-1} are somewhat displaced and expanded compared to the original composition, these are connected to the system's anharmonic potential's asymmetrical vibration [115]. In AB_2O_4 ferrites, AO_4 tetrahedra often have modes above 600 cm^{-1}, while octahedral BO_6 typically has modes below 600 cm^{-1}, as reported by Veronica et al. [116]. The tetrahedral coordination's equal elongation of oxygen atoms along metal–oxygen links causes $A_{1\,g}$ mode. E_g results from the oxygen's symmetric bending with the metal ion in the AO_4 unit, while $T_{2\,g\,(1)}$ results from the tetrahedron's translational movement. $T_{2\,g\,(2)}$ results from uneven stretching of metal and oxygen of the octahedral group, whereas $T_{2\,g\,(3)}$ is induced by asymmetric bending of oxygen. The Raman patterns in the spectrum (Fig. 8) appeared to be doubled because of the inversion; this is especially noticeable when viewing the $A_{1\,g}$ mode. The degree of inversion is correlated with the mode intensities [117]. The $A_{1\,g}$ modes of Fe–O bonding at the bipyramidal 2b site and the tetrahedral 4f1 site were responsible for the 607 and 683 cm^{-1} peak values, respectively. $E_{1\,g}$ vibrations were responsible for the peaks at 205, 204, 210 and 233 cm^{-1}, and $E_{2\,g}$ vibrations were responsible for the peaks at 310, 319, and 329 cm^{-1} [118]. For spinel ferrites, Raman movement is usually observed between 300 and 600 cm^{-1}, with expanded characteristics peaking between 630 and 690 cm^{-1}, overriding the primary $A_{1\,g}$ Raman mode. This behaviour was seen in silver samples, and it may be related to the plasmonic effects of Ag nanoparticles producing a surface-enhanced raman spectroscopy-like effect that is applied to conquer weak scattering [119, 120].

3.3 Magnetic, dielectric and ferroelectric behavior

3.3.1 Vibrating sample magnetometer (VSM)

Using VSM, the M-H hysteresis loops obtained for Ag-substituted nanoparticles and $BaFe_2O_4$ were analyzed for their magnetic characteristics, presented in Fig. 9. Table 5 shows how the magnetization of both kinds of remanent and saturation, coercivity, and squareness ratio was determined by an applied field of around 1 T at room temperature. $BaFe_2O_4$ particles were calculated to have a saturation magnetization of 1.4 emu/g and a retentivity of 0.8 emu/g. This pure sample had a coercivity of 2038 Oe. Table 5 also shows that for the sample $Ba_{0.8}Ag_{0.2}Fe_2O_4$, squareness ratio, retentivity, as well as saturated magnetization were all increased to 0.60, 3.9 emu/g and 6.6 emu/g, respectively, with a decreased coercivity of 1820 Oe. At the same time, the coercivity was further decreased to 1587 Oe for the sample $Ba_{0.7}Ag_{0.3}Fe_2O_4$ having remanent magnetization with 8.4 emu/g and 14.5 emu/g saturation magnetization. It demonstrated that magnetic characteristics improved as Ag concentration increased [121, 122]. In the sample $Ba_{0.5}Ag_{0.5}Fe_2O_4$, the coercivity grew once again with a value of 1731 Oe while the M_s value increased once more to 22 emu/g with rising remanent magnetization of 12.3 emu/g tagging highest among all the samples. For each sample, the residual ratio followed random trends. Improvements in the sample's magnetization and coercivity (Ag = 0.5) concentration demonstrated that it had the best ferromagnetic characteristics. At lesser sizes, stated to be 100–300 nm, single-domain behaviour can be seen in barium ferrite nanoparticles. Unlike larger particles that might change into multi-domain structures, the particle in this condition functions as an isolated magnetic entity, which might increase magnetism [123]. Ag infusion may disrupt the super exchange interactions among Fe ions in both octahedral and tetra sites by affecting the $Fe3^+/Fe2^+$ ratio. This results in improved saturation magnetization (M_s) by altering the magnetic interactions and changing the charge ordering [124]. A reduction of magneto crystalline anisotropy may result from structural distortions or an increase in Fe^{2+} concentration, as indicated by a drop in coercivity (Hc) with Ag substitution. A core–shell magnetic structure may also be induced by Ag inclusion, which could affect interchange bias effects at the boundaries of grains. Ag incorporated may result in oxygen vacancies and defects that alter localized spin interactions and promote $Fe2^+/Fe3^+$ exchange, improving magnetic softness. These flaws might also serve as pinning centers, affecting the coercivity and motion of the domain wall.

The other factor of surface-to-volume ratio also dramatically rises as the particle size falls. This increased surface area may result in improved surface magnetic interactions, which may favorably affect the magnetization as a whole [125]. Therefore, a decrease in particle size combined with structural improvement from Ag substitution would be the determining factor for improved magnetic characteristics. According to previous research, microstructure also affects the hysteresis curve's size and shape, including magnetization and coercivity. The increased magnetic behaviour with substitution demonstrated greater homogeneity and structural density while reducing particle size [126, 127]. However, the relationship between crystal size and coercivity is frequently ambiguous in the case of sol–gel-produced barium ferrite nanoparticles because these magnetic properties depend on the synthesis method, the temperature at which it is annealed, and particle or grain size. In the current study, all samples underwent a 4-h annealing process at 950 °C. With increasing concentration of Ag, the average particle/grain sizes were reduced from 229 to 22 nm and the crystallite size from 43 nm to 24.5 nm according to XRD and SEM examination [128, 129]. The magnetism of ions in both tetrahedral and octa lattice locations is the source of magnetization in spinel ferrites. This distribution of cations and, consequently, the characteristics are significantly impacted by the production technique, annealing temperature, and substitution procedure as reported [130].

According to reports, When Ag^+ ions are added to the host system, they frequently take up positions that host ions would normally occupy. Because Ag^+ has a larger ionic radius than $Ba2^+$, this substitution resulted in an increase in interatomic distances, which may impact the lengths of bonds and angles that are crucial for magnetic interactions aligning with super exchange Goodenough Kanamori rule [131]. In ferrites, spin canting lowers net magnetization. This canting is probably lessened by Ag incorporated, which makes the Fe^{2+} moments more parallel and raises Ms. This is consistent with the Yafet-Kittel hypothesis $M_s \propto Cos\theta$ which states that larger magnetization is the result of a decrease in canting angle θ. Larger grains soften the magnetic response by reducing pinning sites, in accordance with Herzer's hypothesis given as $H_c \propto \frac{K1}{M_s}$. Coercivity would have dropped if initial incorporation had lowered K1 as observed from pristine to Ag = 0.3. As a result, the thermal impact caused the coercivity to drop as the crystallite size decreased. Since the Ag substituted samples'crystallite sizes fall within a single domain, coercivity decreases as

Table 6 Measured magnetic parameters of barium ferrite and silver-infused nanoparticles

Material	Ms (emu/g)	Mr (emu/g)	S = Mr/Ms	Hc (Oe)
$BaFe_2O_4$	1.4	0.8	0.57	2038
$Ba_{0.8}Ag_{0.2}Fe_2O_4$	6.6	3.9	0.60	1820
$Ba_{0.7}Ag_{0.3}Fe_2O_4$	14.5	8.4	0.58	1587
$Ba_{0.5}Ag_{0.5}Fe_2O_4$	22	12.3	0.55	1731

crystallite size decreases following the relation $H_c = g\frac{h}{D^2}$ with D and H_c crystallite size and coercivity while g and h are constants [132].

The material's microstructure also affected the area and form of the curve of hysteresis that combines coercivity and magnetism [133]. As a result, it was discovered that the coercive power, magnetism, and retentivity of barium ferrite nanoparticles produced using the gel-to-glassy and sol–gel processes were the highest, respectively. However, it was found that these magnetic traits were at their lowest during mechanical alloying and combustion processes, as described [134]. Conclusively, saturation magnetization may also be impacted by the composition and synthesis process (e.g., changing the iron-to-barium ratio). For instance, by increasing crystallinity and decreasing defects, improving these factors during synthesis might result in better magnetic characteristics in smaller particles [135] (Table 6).

3.3.2 Dielectric properties

The dielectric characteristics of barium ferrite and Ag-substituted nanoparticles have been studied at room temperature. The results are depicted in Fig. 10a–f. In comparison to $Ba_{0.8}Ag_{0.2}Fe_2O_4$ and $Ba_{0.7}Ag_{0.3}Fe_2O_4$ samples, it was found that the real part of the dielectric constant (ε') (Fig. 10a) of pure BaF and $Ba_{0.5}Ag_{0.5}Fe_2O_4$ was higher at low frequency and lower at high frequency. The conduction mechanism, increased charge carrier mobility, and higher pressure are all thought to be the causes of this phenomenon [136]. Contrary to all Ag substituted samples, the imaginary part of dielectric constant (ε'') (Fig. 10b) and tangent loss (δ) of dielectric (Fig. 10c) of pure BaF were larger at low frequency but decreased as frequency increased. This behaviour could be explained due to the dominance of relaxation-type dielectric action at low frequencies. Depending on the material and circumstances, there can be a wide range of relationships between the frequency and dielectric constant for nanoparticles [137]. A Koops phenomenological theory could explain why the dielectric constant decreases with frequency. According to theory, the drop in polarization and the difficulty of the conductive particles and boundaries of grains complying with the changing field at higher frequencies cause the dielectric constant to fall with frequency. Polarization of space charge evident at low frequencies, resulting from the buildup of charges at flaws and grain boundaries. Confirmation of interfacial polarization effects was seen by the greater dielectric constant at low frequencies from pristine to high concentrated Ag sample [138].

Ferrites'non-conducting grain boundaries interfere with the mobility of charges when an electric field is applied [139]. So, in barium ferrite samples with increasing amounts of Ag substitution, the dielectric loss likewise decreased and then increased. The possibility of a material exhibiting ferroelectricity would also decrease with increasing dielectric loss.

Of all the samples, the sample of Ag = 0.3 showed the best dielectric characteristics (Fig. 10). The material's capacity for preserving electrical power in an electric field is indicated by the real component of the electric modulus (M') in Fig. 10d, e relates to the material's energy storage capacity. However, the imaginary part of the electric modulus (M") represents the transformation of electrical energy into heat and is connected to the material's internal energy dissipation or loss. Pure samples showed better storage capacity but with minor differences, and the dissipation loss in substituted samples was less, which is useful. Figure 10f presents a Cole–Cole plot for all the samples'relative behaviour. The imaginary axis represents the material's conductivity, and the real axis represents its static dielectric constant. Polarization in dipolar connected to the unequal distribution of charges in Fe^{2+}/Fe^{3+} ions in $BaFe_2O_4$ influenced dielectric dispersion and exhibited relaxation behavior in the Cole–Cole plot as shown in Fig. 10f. The Cole–Cole plot is an invaluable tool for comprehending dielectric materials and their properties in the framework of ferroelectrics and other materials with complicated dielectric behaviour. It is employed in the analysis of materials'dielectric relaxation [140]. The broader or more erratic semicircle implies many relaxation periods or a spread of relaxation times, and a well-defined semicircle implies a single relaxation time in substituted samples. It can be observed that polarization of ions originated when an external field caused the Ba^{2+}, Fe^{2+}, and O^{2+} ions to be displaced and deduced from the examination of the electric modulus, where ion migration effects are indicated by relaxation peaks. The adaptation of the dielectric characteristics

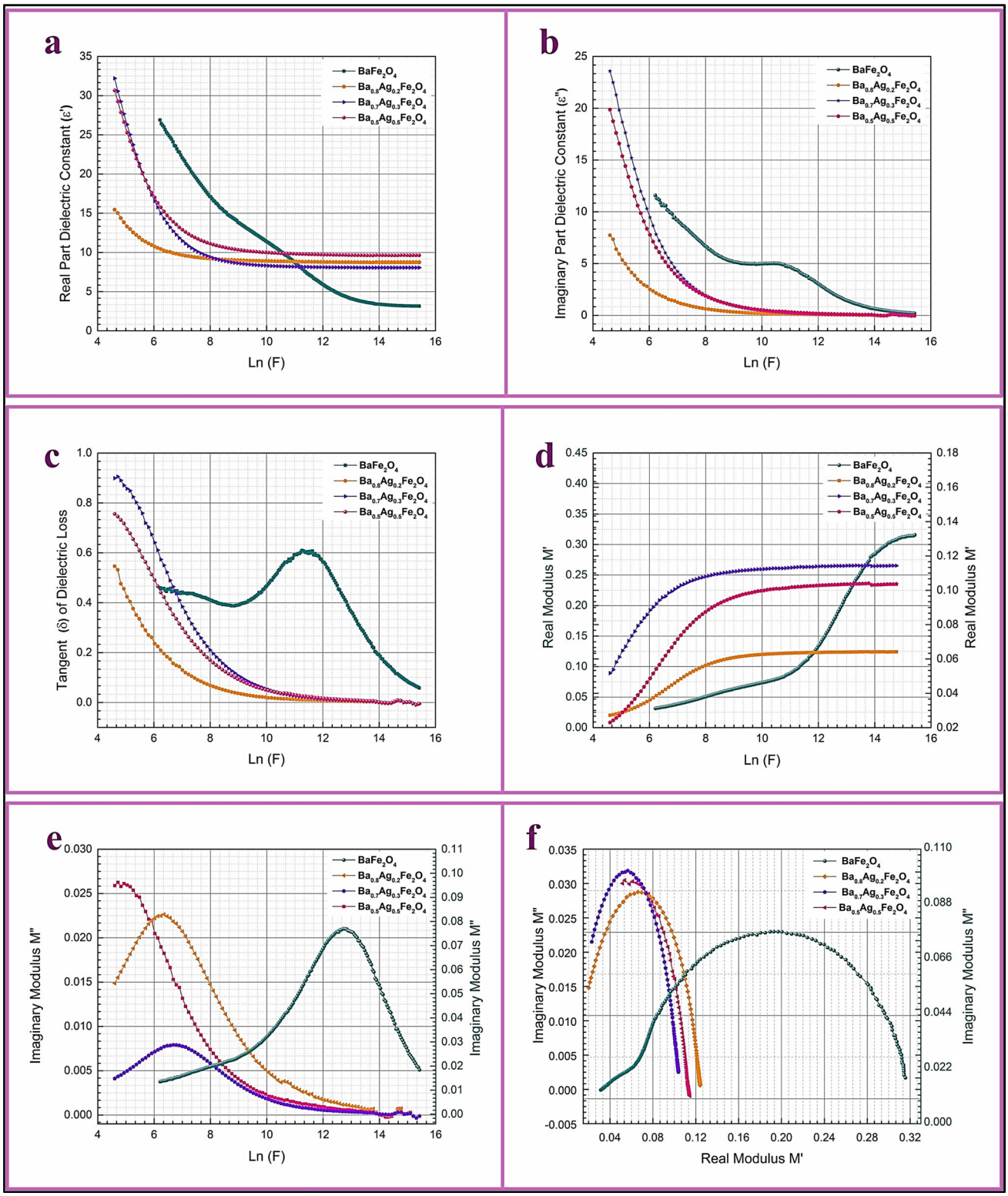

Fig. 10 Measured dielectric properties **a** real part dielectric constant **b** imaginary part dielectric constant **c** dielectric loss **d** real electric modulus **e** imaginary electric modulus **f** cole–cole plot of pristine barium ferrite and silver substituted nanoparticles

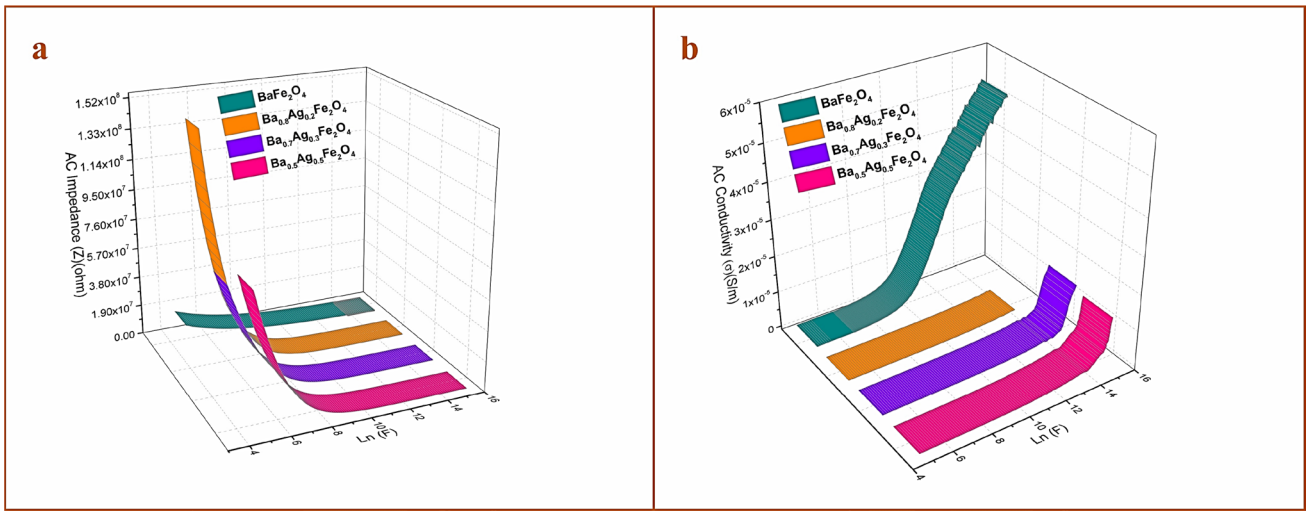

Fig. 11 AC impedance and AC conductivity of pristine and silver-substituted barium ferrite nanoparticles

as vacancies of oxygen in the sample may have decreased while increasing the concentration of Ag might be attributed to the phenomenon of dielectric relaxation. According to reports [141], the size of the reduction nanoparticle and the phenomenon of bounce conduction involving Fe^{3+} and Fe^{+2} ions in ferrites affected the dielectric characteristics.

The AC impedance and conductivity are also shown in Fig. 11a, b. In the context of magnetic nanoparticles, impedance can provide insight into the charge carrier mobility and interfacial properties. Important information for PV applications, such as polarization effects, relaxation durations, and dielectric response, is indicated by the frequency-dependent impedance [142]. On the other hand, defect-assisted transport, band conduction, or tiny polaron hopping are the primary conduction mechanisms that are revealed by temperature-dependent AC conductivity study. A substance's AC conductivity, which is correlated with frequency and impedance, indicates its ability to conduct electricity upon exposure to an alternating electrical field and more AC conductivity usually implies more charge carrier mobility. It was also possible to see an inverse relationship between AC conductivity and AC impedance. While the impedance is larger at low frequencies and decreases at high frequencies, the AC conductivity increases with the frequency trend. The conductivity of the pure sample was good, but it dropped with the subsequent concentration of Ag = 0.2. The AC impedance abruptly changed, becoming lower in pure and Ag = 0.3 and higher in Ag = 0.2 and 0.5. High AC impedance for low frequencies can be linked to grain boundaries. For ferrite nanoparticles, the frequency-dependent impedance spectrum shows that conduction is encouraged by the applied AC field [143]. The current studies were carried out at room temperature, but minimal conductivity and high impedance are recorded at low temperatures. Doping or substituting and particle size control the applied alternating field's ability to boost AC conductivity in magnetic nanoparticles as it rises with frequency [144]. Conductivity rises, and the hopping length falls as the number of ferrous ions on octahedral sites rises, increasing the dielectric constant. The infused foreign element decreases the number of Fe^{2+}/Fe^{3+} ion pairs and the resulting alteration in the cationic distribution, which is influenced by particle size, can be utilized to alter the AC conductivity, which improves with frequency and qualifies the nanoparticles for application in PV [145]. Overall, the material's dielectric properties can influence how charge carriers are carried and separated. Selecting materials with a high dielectric constant can help reduce charge carrier recombination. This is significant because a lowered recombination rate allows more electrons to reach the electrode, increasing the photo voltaic cell's efficiency [146, 147]. All things considered, the infusion of Ag and reduced sizes of particles in barium ferrite changed structural properties which comprise strain in the lattice and dislocation density, which have an immediate impact on AC conductivity, dielectric loss, AC impedance and the dielectric constant. Because the material's dielectric characteristics and microstructural characteristics are closely related, these modifications can increase the material's suitability for specific high-frequency applications [148].

3.3.3 Multiferroic system

Using the Multiferroic system, the pristine barium ferrite and Ag substituted (x = 0.2, 0.3, 0.5) samples were analyzed at room temperature. The samples were taken in the form of free-standing films prepared by solution casting method as

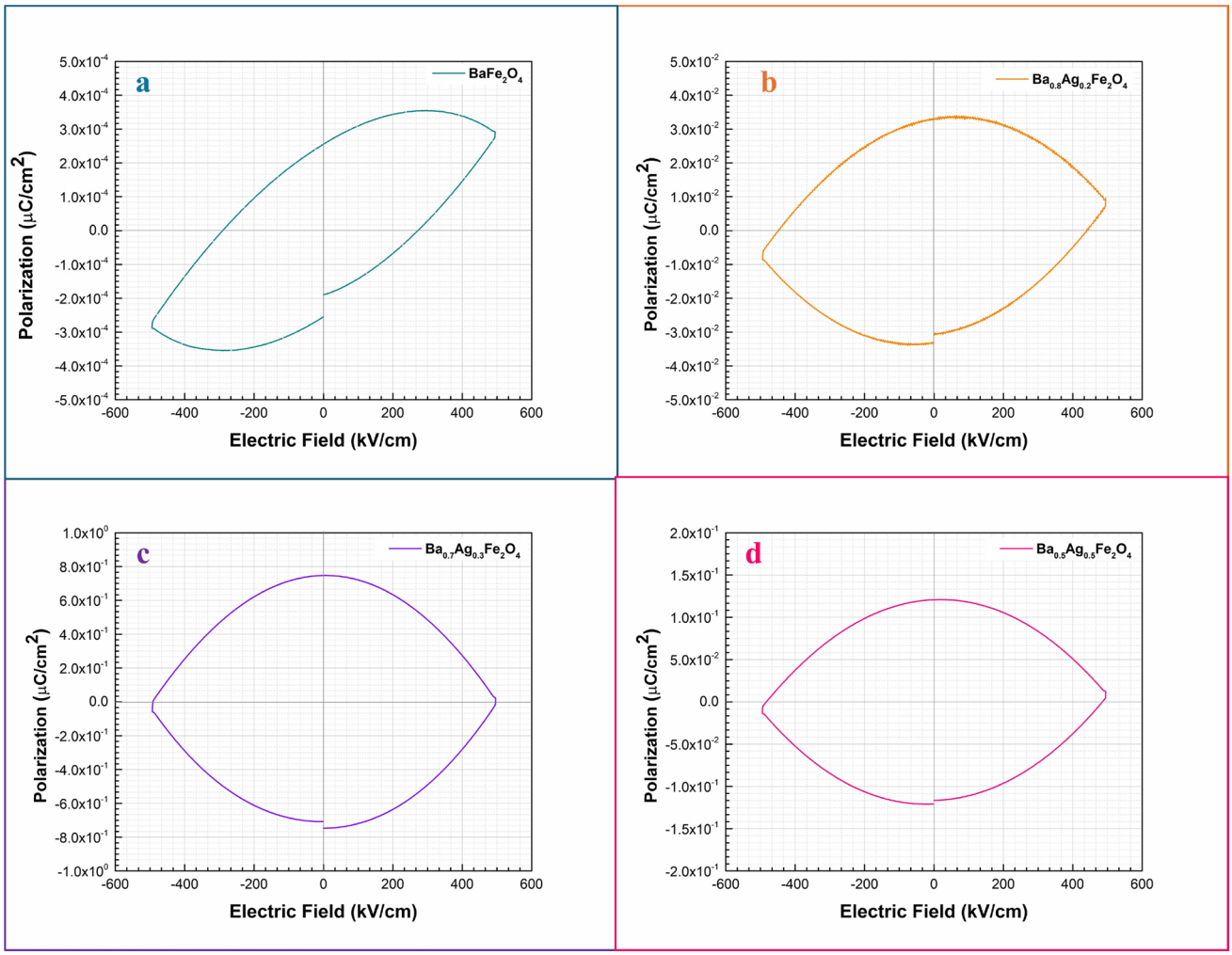

Fig. 12 PE loops for pristine and silver substituted barium ferrite nanoparticles at room temperature

per the requirement of a multiferroic system used. The ferroelectric nature of the samples shown in Fig. 12a–d was verified for each sample independently by (P-E) loops that are polarization and electric field hysteresis.

Good ferroelectric behaviour was indicated by Fig. 12a, which showed a clearly defined hysteresis loop with comparatively large polarization values. In Fig. 12b, the loop is not as defined and the value of polarization are much lower than the pristine one. As polarization further diminishes in Fig. 12c and the loop grows more linear, it may indicate a higher leakage or conduction current. In part 12 d, the loop approaches total linearity, which is similar to the behaviour of a material with conductivity with little ferroelectricity or a lossy dielectric. For conduction analysis, the polarization values drop as the hysteresis loops get more linear from the pristine sample to Ag ($x = 0.5$). This implies that the samples' conductivity (or leakage current) is gradually rising. Since conduction paths dominate the material's response, a linear loop with less polarization indicates more conduction and less ferroelectric property [149]. Increased electrical conductivity results from charge carriers moving more freely in materials where conduction channels predominate. This is frequently seen in material that has changed from ferroelectric to more conductive states when charge carrier mobility overcomes polarization's effects [150]. Ferroelectrics usually show hysteresis loops, which are typified by a persistent polarization upon removal of the external field. Materials with low polarization, on the other hand, lose this distinctive behaviour, indicating a shift to a phase where conduction predominates. Ferroelectric materials offer an inside electric field (caused by polarization) that facilitates charge separation and improves photovoltaic performance, making them attractive for PV applications [151]. The decreasing polarization and progressive linear loops show that the samples'conduction rises from pristine to the highest concentration of silver substituted. Sample A's low conduction and strong ferroelectric characteristics make it the ideal option for photovoltaic applications. But the magnetization of samples was increased from ($x = 0.0$) to ($x = 0.5$). Stronger

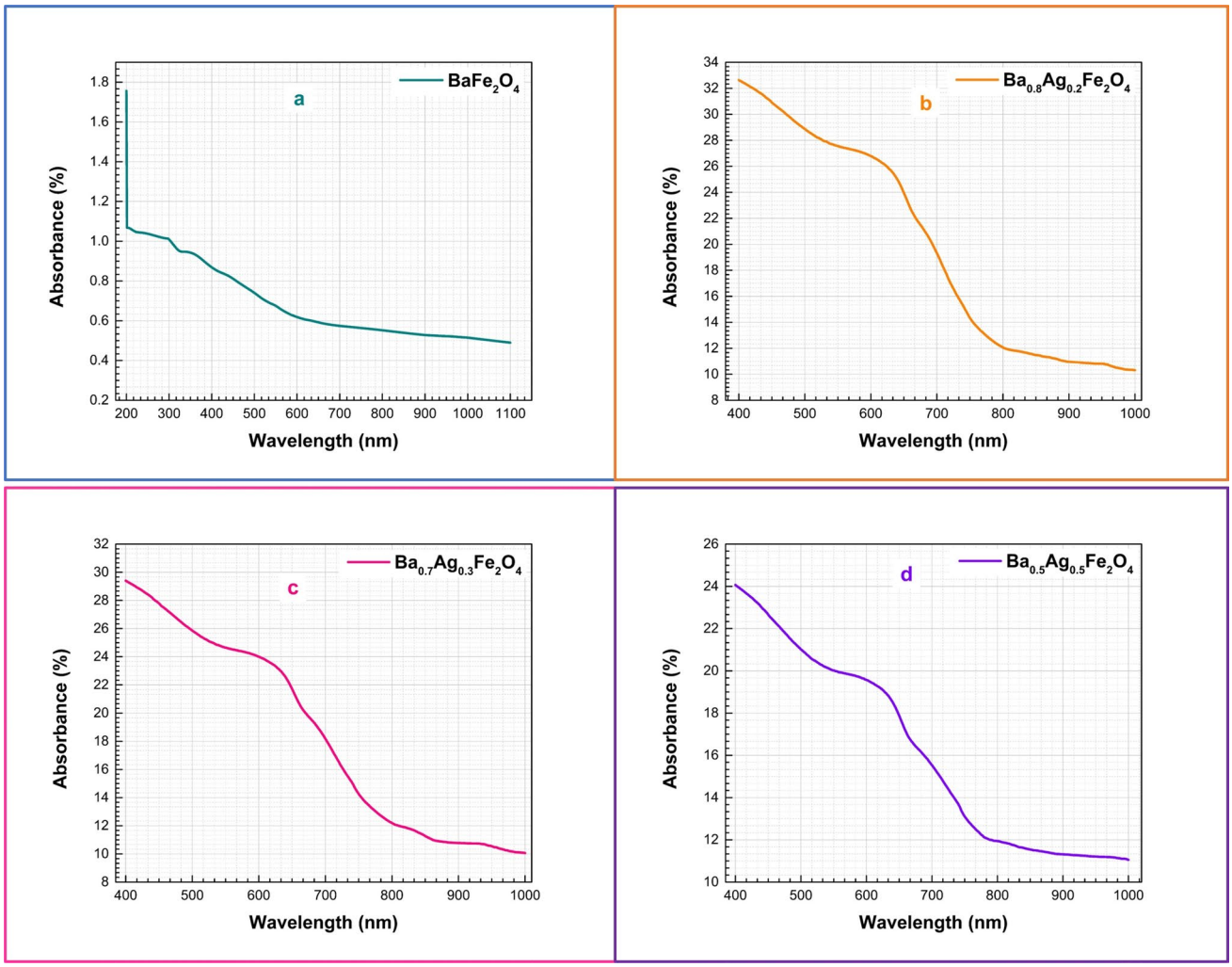

Fig. 13 Measured absorbance of barium ferrite and silver substituted nanoparticles

ferromagnetic behaviour was shown by increasing magnetization, while ferroelectric characteristics deteriorated as demonstrated by the smaller polarization loops. The efficiency of ferroelectricity for PV applications may be decreased by higher conduction as indicated by the PE loop for the sample Ag (x = 0.5). Higher magnetization may improve some magnetic capabilities, but it may also result in leakage currents, which would be bad for PV performance. The advantages of magnetization may be overshadowed by short-circuiting the device due to excessive conduction channels. Because of their special polarization characteristics, ferroelectric materials are renowned for their capacity to produce high open-circuit voltages. By raising the voltage supply under illumination, a feature can improve the effectiveness of solar cells, which is advantageous for PV applications [152]. Furthermore, the crystal structure—including imperfections and anisotropic of single or multiple domains—determines the overall magnetized and polarized properties of the nanoparticles. In our instance, fewer nanoparticles resulted in higher magnetization. This suggests that reduced polarization due to size-based restrictions on smaller nanoparticles may impair the material's ability to maintain a stable polar structure [153].

So, it can be concluded that a decrease in ferroelectricity and higher conduction in Ag (x = 0.3) and (x = 0.5) reduce the ideal value for PV applications, even if magnetism increases. The optimal compromise was found in a pristine barium ferrite sample, which maintains controllable conduction levels while supplying enough ferroelectricity for efficient charge separation. As a compromise, Ag (x = 0.2) may also merit more investigation if magnetoelectric coupling plays a role. The continuing research of ferroelectric material optimization research for photovoltaic applications is to balance polarization and conductivity. To maximize photocurrent production and overall device efficiency, this balance must be struck [154].

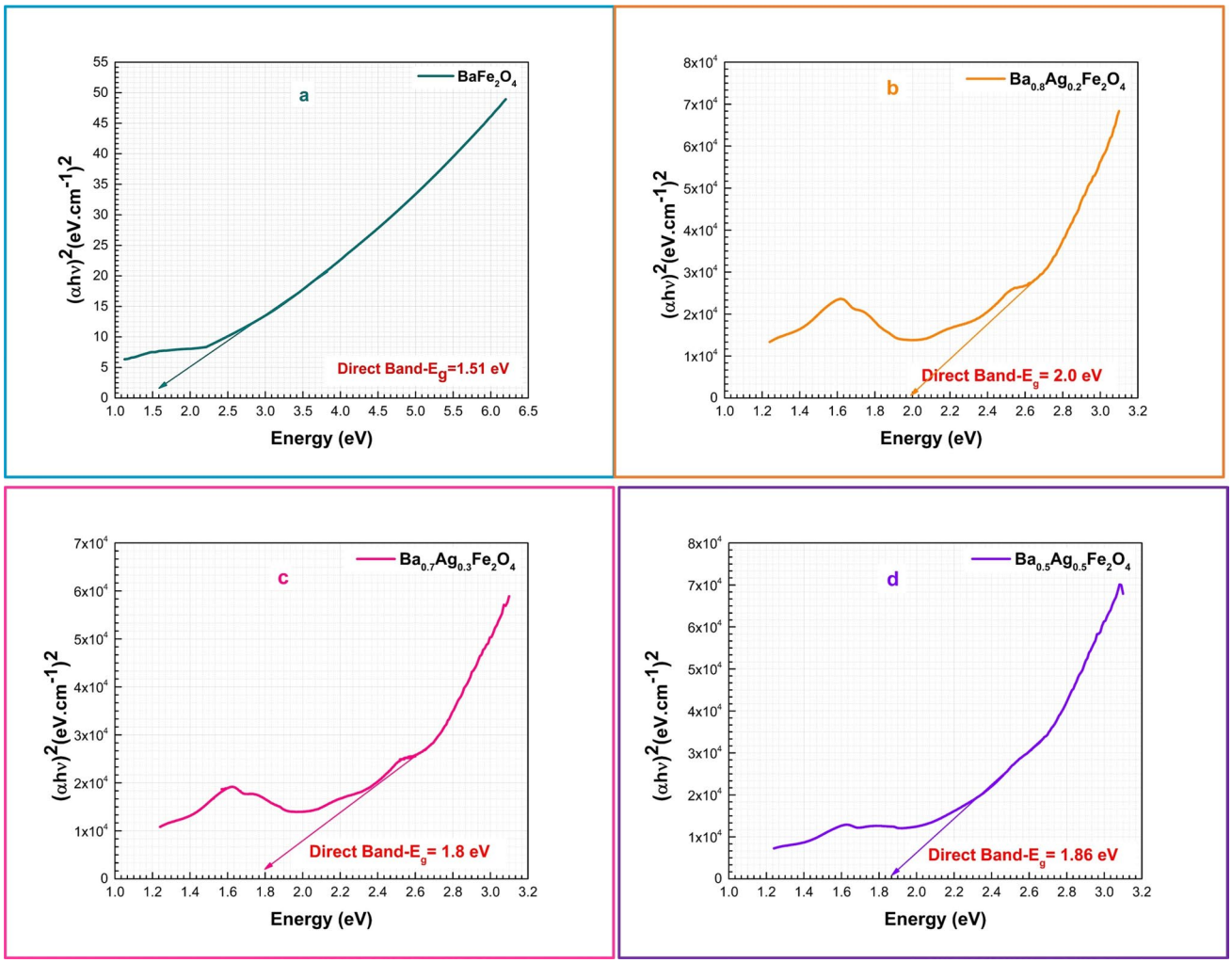

Fig. 14 Calculated energy band gaps of barium ferrite and silver substituted nanoparticles

3.4 Optical and photovoltaic response

3.4.1 UV–visible diffuse reflectance spectroscopy

By using UV–visible spectroscopy, the optical characteristics of absorbency and energy gaps between bands were examined. Figure 13 shows the absorbance spectra of Ag-substituted and pure BaF nanoparticles. The shift in the absorbance curves between 600 and 800 nm was related to the change in electronic structure in the conduction and valence bands. Compared to pure barium ferrite, the absorbance in Ag samples (x = 0.2, 0.3, 0.5) was higher and was observed in the visible spectrum range. Pure $BaFe_2O_4$ had an absorbance of 1.8%, which rose dramatically to 34% with Ag = 0.2. It then progressively dropped to 30% for A = 0.3 and valued 24% for Ag = 0.5. Ag-induced electronic states and improved optical transitions were probably what caused the initial rise in photon absorption. The localized surface plasmon resonance effects could be generated by Ag inclusion, increasing light absorption even more. The development of extra defect states, which increases carrier recombination and lowered absorption efficiency, was responsible for the subsequent drop in absorbance at high incorporated levels [155]. The potential for presence of Ag creation at greater content caused light scattering losses. This phenomenon was typical of substituted oxide materials, where high infusion concentrations cause defect-induced non-radiative recombination to decrease absorption efficiency in many reported studies [156].

Figure 13 (a-d) portrayed the energy levels for all the samples. Direct bands were used to determine the energy bands (E_g). Following is the relationship of Tauc $(\alpha hv)^2 = A\left(hv - E_g\right)$. Here,'A'is absorbance,'A'(absorption coefficient) = 2.303 x

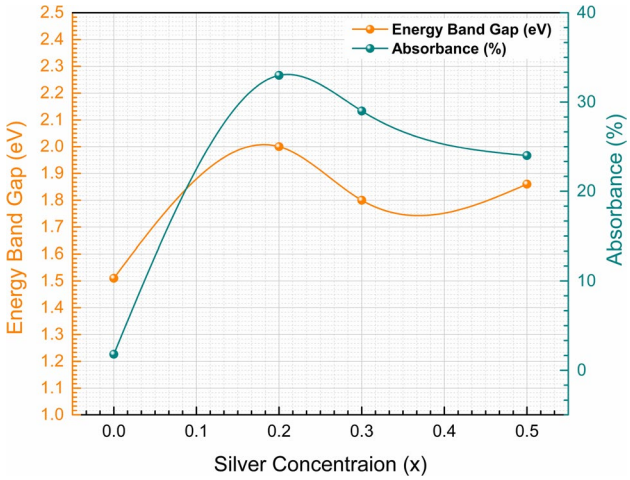

Fig. 15 Deviation of absorbance and energy band gaps with increasing concentrations of silver in barium ferrite nanoparticles

(absorbance)x(energy), and 'hv'(planks constant x the frequency of light) = 1240/wavelength in Eq. 4. Here, 2 = n for the direct band gap. It does, however, have several restrictions and error-prone areas. For modified semiconductors, the Tauc approach, for instance, may provide a reduced estimate of the bandgap energy and result in some inaccurate findings [157, 158].

Figure 14a shows that the straight band gap value of pure $BaFe_2O_4$ was 1.51 eV. For $Ba_{0.8}Ag_{0.2}Fe_2O_4$ and $Ba_{0.7}Ag_{0.3}Fe_2O_4$, the band gap increased to 2.0 eV and then 1.8 eV respectively corresponding to non-monotonic changes. The band gap of $Ba_{0.5}Ag_{0.5}Fe_2O_4$ was again increased by 1.86 eV with an increasing Ag = 0.5 concentration. The sample Ag = 0.3 had the lowest band gap among substituted samples. Figure 15 shows the absorbance (%) and energy bands (eV) divergence due to increasing Ag concentration. Of all the samples, the $Ba_{0.7}Ag_{0.3}Fe_2O_4$ sample with the narrowest band gap exhibited the highest level of light absorption. Ag^+ incorporation modified the electronic structure, possibly inducing cation redistribution or structural distortions that widen the band gap. Stronger $Fe3^+$–O hybridization due to lattice strain may shift conduction/valence bands. Quantum confinement effect due to decreasing crystallite size (43 ⟶ 40 nm) [159, 160]. Defective states such as Ag-Fe disorder and the oxygen occupancy produced mid-gap states at increasing Ag content, which lowered E_g in the sample $Ba_{0.7}Ag_{0.3}Fe_2O_4$ by improving carrier delocalization. As the crystallite size continues to shrink to 35 nm, the band structure can change. On the next when crystallite size grew to 38 nm with the subsequent minor increase afterwards (1.86 eV in Ag = 0.5) was observed largely restoring the previous band structure. The E_g might have been somewhat elevated by secondary phase development or Ag clustering [161].

Additionally, it is stated that the Ag ions drove the Fe^{3+} ions through octahedral points to tetrahedral in the ferrite structure, causing a lattice distortion in the structure that followed increased stresses and lattice constants with decreased band gaps. The electrical structure of materials, especially their band gaps, can be impacted by lattice distortions. Lattice deformation and band gap fluctuation have complicated interactions depending on the type of material used and distortion. Increased lattice distortion can sometimes reduce the band's width while having the opposite effect [162, 163]. The XRD results in Table 1 also supported increased lattice constants and micro strain. Numerous academic studies have investigated how Ag affected the optical characteristics of ferrite nanoparticles. The findings demonstrate that the production technique and Ag concentration affect the optical characteristics [131].

3.4.2 Photoluminescence and fluorescence spectrum

Figure 16a–c shows the photoluminescence spectra of pure and Ag-substituted BaF nanoparticles to support their photovoltaic and optical characteristics. With a wavelength for excitation of 405 nm and an intense power source pulse of 100 kW, the frequency was set at 100 Hz. The range of the emitting window was set at 400 to 780 nm. The PL spectra also have been fitted with gaussian model to precisely deconvolute the emission peaks. A more accurate examination of the material's defect states and recombination mechanisms is made possible by this fitting. Figure 16b possessed the emission spectrum regarding wavelength and concentrated emission intensity measured by fluorescence spectroscopy. The fluorescence mode of this emission measurement revealed the optical material's concentration. All the samples

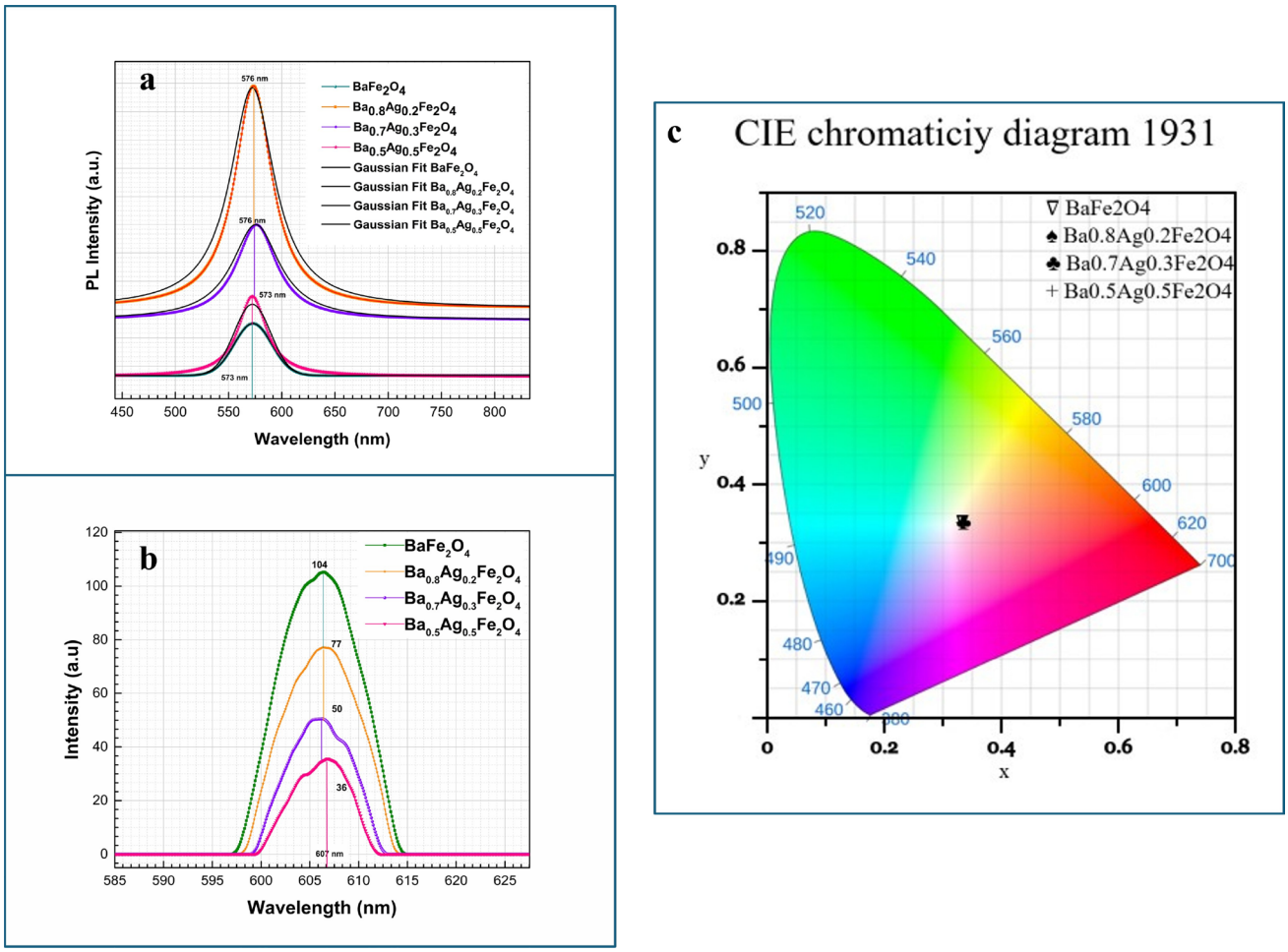

Fig. 16 Photoluminescence spectrum **a** and fluorescence spectrum **b** with emission intensity of barium ferrite and silver substituted particles **c** Chromaticity CIE diagram

reflected the broad emission lines, which were the same in the visible spectrum. $Ba_{0.5}Ag_{0.5}Fe_2O_4$, $Ba_{0.7}Ag_{0.3}Fe_2O_4$, and $Ba_{0.8}Ag_{0.2}Fe_2O_4$ showed 36, 50, and 77 concentrations at 607 nm, respectively. $BaFe_2O_4$ had a strong concentration intensity peak, also seen at 607 nm with a value of 104. $Ba_{0.5}Ag_{0.5}Fe_2O_4$ and $Ba_{0.7}Ag_{0.3}Fe_2O_4$ had minimal emission. The increased material concentration indicates that the arrangement of the structures is highly concentrated within, preventing the solar panel's incident light from being spread evenly. The solar panel may sustain damage from the excited electrons'excessive production of thermal energy when light is always directed at the same spot [164]. On the other hand, in Fig. 16a, when the concentration of Ag was increased from x = 0.3 to 0.5, it seemed to enhance the stimulation of photons in barium ferrite. While the strong peak demonstrated the rapid recombination caused by structural defects with substitution [165], the lower emission intensity indicated a low percentage of the electron- hole pair recombination. Photoluminescence behaviour can be predicted by adjusting ferrite nanoparticles'physical properties, size, and

Table 7 Measured optical properties of barium ferrite and silver-substituted nanoparticles

Materials	Direct Band Gap E_g (eV)	Absorbance (%)	Fluorescence Concentration intensity at 607 nm	Photoluminescence emission at wavelength (nm)
$BaFe_2O_4$	1.51	1.04	104	573 yellow light
$Ba_{0.8}Ag_{0.2}Fe_2O_4$	2.0	33	77	576 yellow light
$Ba_{0.7}Ag_{0.3}Fe_2O_4$	1.8	29	50	576 yellow light
$Ba_{0.5}Ag_{0.5}Fe_2O_4$	1.86	24	36	573 yellow light

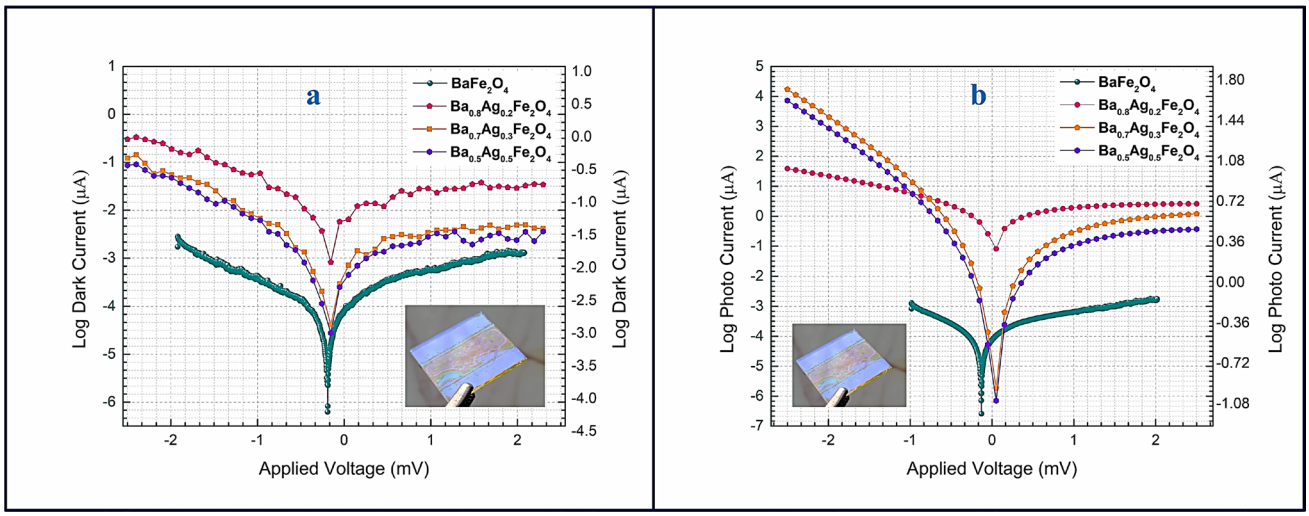

Fig. 17 Dark and photo current of pristine and silver substituted nanoparticles

composition. Due to their adaptability, materials can be created with precise emission wavelengths and intensities, making them useful for photovoltaic applications [166]. Calculated as $\frac{1240}{\lambda} = \frac{1240}{576} = 2.1eV$, the energy band for photons associated with the emission of PL at 573 and 576 nm corresponded to yellow light (Table 7) that was matched to the band gap detected by UV–visible results (Fig. 13). The reported phase change in ferroelectric materials is also responsible for the abrupt increase in the emission intensity of PL spectrum from pure barium ferrite samples to those substituted with Ag. Consequently, the photoluminescence response for the barium ferrite and Ag-substituted samples generated emission in the visible region, which is significant for optical devices [167–170]. A chromaticity diagram from the CIE 1931 version [171] has also been added (Fig. 16c) to show the colorimetric characteristics of the light that is emitted. The CIE diagram offered important information about the possible optoelectronic uses of the materials that were synthesized. A more thorough understanding of the optical characteristics was ensured by these additions, which improved the PL analysis's clarity and comprehensiveness. The charge carrier activities within the material are influenced by the size of the crystallite and optical characteristics as well, which were strongly related to the change in PL intensity of emission across various compositions. Because it predicted longer-lived charge carriers, the pure sample's $BaFe_2O_4$ comparatively lower PL emission intensity at 573 nm suggested a lower rate of radiative recombination, which is advantageous for photovoltaic applications [172, 173].

The $Ba_{0.8}Ag_{0.2}Fe_2O_4$ composition had the maximum PL intensity at 576 nm after Ag substitution, indicating a boost in centers of recombination that might result in improved electron–hole pair annihilation. At 576 nm, the $Ba_{0.7}Ag_{0.3}Fe_2O_4$ showed somewhat lower intensity, indicating either better charge separation or a potential decrease in non-radiative defects. The $Ba_{0.5}Ag_{0.5}Fe_2O_4$ sample eventually returned to a reduced PL emission at 573 nm, which was comparable to the pristine sample. This advocated that charge carrier dynamics have recovered, favoring photovoltaic performance. This pattern was consistent with the reported variation in crystallite size, where a reduction in size generally increases defect-related recombination and quantum confinement effects. The Ba sample with Ag = 0.3 concentration seemed to be the most promising option for photovoltaic applications because its band gap of 1.8 eV is closer to the optimal range for the absorption of sunlight (1.1–1.9 eV) and provided the best steadiness between reduced recombination losses and charge separation while maintaining carrier lifetime [174]. In addition, this sample maintained a higher absorbance than the Ag = 0.5, which guaranteed improved visible light collection with a size of 35 nm, might offering a good dispersion of grain boundaries, lowering recombination losses while allowing for efficient charge transfer.

3.4.3 Photo current measurement

By evaluating I-V characteristics by using a solar simulator (AM 1.5G filter standard) with 1 SUN output power at room temperature, the PL effect and the reduction of band gaps on the photovoltaic behaviour of pure BaF and Ag substituted nanoparticles were investigated and shown to Fig. 17a, 16b. The nanoparticles were deposited as thin films and tested as part of the I-V testing process. The active material, PVA, cetyltrimethylammonium bromide CTAB and DI water were

Table 8 Photovoltaic characteristics under illumination of pristine and silver substituted NPs deposited thin films

Compound Samples	V_{oc} (mV)	I_{sc} (μA)	Fill Factor $(FF) = \frac{V_m \times I_m}{V_{oc} \times I_{sc}}$
ITO	− 0.09	0.083	≈ 0.3–0.8
$BaFe_2O_4$	− 1.93	0.116	0.14810
$Ba_{0.8}Ag_{0.2}Fe_2O_4$	0.6	− 0.125	0.69444
$Ba_{0.7}Ag_{0.3}Fe_2O_4$	0.65	− 0.111	0.71394
$Ba_{0.5}Ag_{0.5}Fe_2O_4$	0.7	− 0.097	0.734693

combined to create a solution in the first stage. Thin films were prepared using spin coating with 2000 rpm and 60 s after the uniform slurry of the nanoparticles was applied to the conductive side of ITO glass, which was chosen as the photoanode substrate. The three layers were deposited with small intervals of gap. The films had an active area of 2×1 cm^2 out of a total slide of 2×2 cm^2, and masking tape was used to cover the remaining substrate area. To establish good adhesion after evaporating the solvent, the films were initially allowed to air dry before being put in the heating oven at 100°C for a few minutes. After that, each film was annealed at 250°C for 1 h in the muffle furnace to achieve a good structure. At a voltage being applied of 100 mV, the standard values for I-V curves were initially obtained using simply ITO glass with no active coating, and the voltage frame was set from −2.00 to 2.00. The measurement result was used as the substrate's reference value. The ready films of each sample pristine to (x = 0.5) were then taken one at a time, and the current–voltage curves were analyzed using the solar simulator system's two probes by connecting the electrical contacts.

The I-V characteristics of Ag substituted thin films and pristine BaF for the dark current without illuminating light on processed films are shown in Fig. 17a. With a modest depth current, the photovoltaic behaviour curves were visible. The curves for photocurrent in the occurrence of a visible light source are shown in Fig. 17b. The concept of producing current by activation of photons through the outermost layer of pure BaF and increasing Ag concentration thin films was implemented. The films $Ba_{0.8}Ag_{0.2}Fe_2O_4$ and $Ba_{0.5}Ag_{0.5}Fe_2O_4$ generated a higher photocurrent than others. The open-circuit voltage is shown on the graph at the position when the current is zero. Better performance is typically indicated by a higher V_{oc} since it allows the solar cell to produce a greater voltage differential, which increases power output. The short-circuit current is shown on the graph at the point when the voltage is zero. The solar cell may produce more current when its I_{sc} is higher, which also increases its power production. The fill factor (FF) is higher when the current–voltage curve near the maximum power point (MPP) is steeper. The FF indicates the degree to which the power output of the PV cell reaches its theoretical maximum [175]. Table 8 shows the photovoltaic attributes, such as short circuit current (I_{sc}) and open circuit voltage (V_{oc}), which were assessed using photovoltaic analysis utilizing EC Lab software.

According to reports, when the ferro magnetic material was exposed to the applied voltage, the dipole moment was boosted, increasing the current that is induced and efficiency. The phase change, dielectric constant, and coercivity are also linked to the induction of charges in photo-ferroelectric materials. Since the internal domain will align appropriately, the slight dielectric losses and constant may increase the induced current [42, 176]. This study attempted to investigate low band gaps and the photovoltaic response of barium ferrite nanoparticles with Ag substitution, which may be considered to contribute to the development of carefully considered photo ferromagnetic materials for solar applications.

4 Conclusions

In this study, pure $BaFe_2O_4$ nanoparticles that had increasing concentrations of Ag substitution (x = 0.2, 0.3, and 0.5) were successfully synthesized by sol gel method. The incorporation of Ag was efficiently observed improving all the examined properties for the application. The nanoparticle's size decreased from 46–35 nm with marginal strain and grain size was reduced from 229 to 22 nm revealing the influence of Ag on carrier mobility, influencing the optical, magnetic properties. Substitution reduced coercivity while increasing the magnetization from about 1.4 emu/g to 22 emu/g, upgrading the strong magnetic collaborations with Ag presence. Ag substituted $BaFe_2O_4$ achieved an adjustable band gap (1.5–2.0 eV), while light absorbing capacities were improved by a considerable increase in absorbance from 1.8% to 34% which allowed the nanoparticles for effective solar energy absorption—a crucial component of photovoltaic applications. $Ba_{0.7}Ag_{0.3}Fe_2O_4$ that depicted the ideal value of 1.8 eV band gap. Higher Ag concentrations caused PL quenching, which indicated less charge carrier recombination and encouraged photogenerated current efficiency exhibiting the emission

spectrum at a visible wavelength of 573–576 nm, a yellow light region ideal for PV devices, and the lowering fluorescence concentration with substitution of silver showing material's suitability for the application. The substantial leakage current that was detected by PE loops emphasized the necessity of additional electrical property optimization prior to the manufacturing of a workable device. Pure sample $BaFe_2O_4$ had the highest photocurrent, according to photovoltaic testing, whereas $Ba_{0.8}Ag_{0.2}Fe_2O_4$ had the second-highest I_{sc} value and the same current density trend. The material's potential as a photoactive material in PV devices highlighted by the improved photocurrent at optimal Ag concentration of x = 0.2 which validated better charge separation. Based on assessed attributes from all the measured properties compared to other previously researched ferroelectric and magnetic materials, this study attempted to present the barium mono ferrite $BaFe_2O_4$ as a potential material for photovoltaic applications. To improve electrical performance and confirm its effectiveness in actual solar device, more research is needed.

Acknowledgements The authors acknowledge the School of Chemical and Materials Engineering (SCME), at National University of Sciences and Technology (NUST), Islamabad, Pakistan for all the administrative and financial support.

Author contributions Irum Shahid Khan (first author) wrote and collected scientific data and performed the analysis. Iftikhar Hussain Gul (corresponding author) reviewed the whole work.

Funding This research received no specific grant from public, commercial, or not-for-profit funding agencies.

Data availability All the generated or analyzed data during this study are included in this published article. No additional datasets were generated or required for this research as all relevant data is fully presented and published within the article.

Declarations

Ethics approval and consent to participate Not applicable.

Consent for publication Not applicable.

Competing interests The authors declare no competing interests.

References

1. Gielen D, Boshell F, Saygin D, Bazilian MD, Wagner N, Gorini R. The role of renewable energy in the global energy transformation. Energ Strat Rev. 2019;24:38–50. https://doi.org/10.1016/J.ESR.2019.01.006.
2. Jacobson MZ. Review of solutions to global warming, air pollution, and energy security. Energy Environ Sci. 2009;2(2):148–73. https://doi.org/10.1039/B809990C.
3. Jerez S, et al. The impact of climate change on photovoltaic power generation in Europe. Nat Commun. 2015;6(1):1–8. https://doi.org/10.1038/ncomms10014.
4. Narvaez G, Giraldo LF, Bressan M, Pantoja A. The impact of climate change on photovoltaic power potential in Southwestern Colombia. Heliyon. 2022;8(10): e11122. https://doi.org/10.1016/J.HELIYON.2022.E11122.
5. Abou Jieb Y, Hossain E. Photovoltaic systems. Cham: Springer International Publishing; 2022. https://doi.org/10.1007/978-3-030-89780-2.
6. Mousazadeh H, Keyhani A, Javadi A, Mobli H, Abrinia K, Sharifi A. A review of principle and sun-tracking methods for maximizing solar systems output. Renew Sustain Energy Rev. 2009;13(8):1800–18. https://doi.org/10.1016/j.rser.2009.01.022.
7. E. Bravo, Nanoparticle-based Solar Cells EE453 Project Report submitted by.
8. Wang L, et al. A holistic and state-of-the-art review of nanotechnology in solar cells. Sustainable Energy Technol Assess. 2022;54: 102864. https://doi.org/10.1016/j.seta.2022.102864.
9. Moon SH, et al. Monolithic DSSC/CIGS tandem solar cell fabricated by a solution process. Sci Rep. 2015;5(1):1–6. https://doi.org/10.1038/srep08970.
10. Nguyen HL, et al. Effects of growth temperature on the morphological, structural, and electrical properties of CIGS Thin Film for use in solar cell applications. Energies. 2023;16(11):4467. https://doi.org/10.3390/en16114467.

11. Kishore Kumar D, et al. Functionalized metal oxide nanoparticles for efficient dye-sensitized solar cells (DSSCs): a review. Mater Sci Energy Technol. 2020;3:472–81. https://doi.org/10.1016/j.mset.2020.03.003.
12. Sutherland BR. Solar materials find their band gap. Joule. 2020;4(5):984–5. https://doi.org/10.1016/j.joule.2020.05.001.
13. Sharma S, An overview on ferroelectric photovoltaic materials, sustainable material solutions for solar energy technologies: processing techniques and applications, pp. 175–199, 2021, https://doi.org/10.1016/B978-0-12-821592-0.00002-9.
14. Kumari T, et al. A built-in electric field induced by ferroelectrics increases halogen-free organic solar cell efficiency in various device types. Nano Energy. 2020;68: 104327. https://doi.org/10.1016/J.NANOEN.2019.104327.
15. Han X, Ji Y, Yang Y. Ferroelectric photovoltaic materials and devices. Adv Funct Mater. 2022. https://doi.org/10.1002/adfm.202109625.
16. Zhang J, et al. Enlarging photovoltaic effect: combination of classic photoelectric and ferroelectric photovoltaic effects. Sci Rep. 2013;3(1):2109. https://doi.org/10.1038/srep02109.
17. Grinberg I, et al. Perovskite oxides for visible-light-absorbing ferroelectric and photovoltaic materials. Nature. 2013;503(7477):509–12. https://doi.org/10.1038/nature12622.
18. Yi HT, Choi T, Choi SG, Oh YS, Cheong S-W. Mechanism of the switchable photovoltaic effect in ferroelectric $BiFeO_3$. Adv Mater. 2011;23(30):3403–7. https://doi.org/10.1002/adma.201100805.
19. Ma N, Zhang K, Yang Y. Photovoltaic–pyroelectric coupled effect induced electricity for self-powered photodetector system. Adv Mater. 2017. https://doi.org/10.1002/adma.201703694.
20. Eskandari R, Zhang X, Malkinski LM. Polarization-dependent photovoltaic effect in ferroelectric-semiconductor system. Appl Phys Lett. 2017. https://doi.org/10.1063/1.4978749.
21. Qin M, Yao K, Liang YC. High efficient photovoltaics in nanoscaled ferroelectric thin films. Appl Phys Lett. 2008. https://doi.org/10.1063/1.2990754.
22. Wang C, et al. Photocathodic behavior of ferroelectric Pb(Zr, Ti) O3 films decorated with silver nanoparticles. Chem Commun. 2013;49(36):3769. https://doi.org/10.1039/c3cc38545k.
23. Laurenti M, et al. Nanobranched ZnO structure: p-type doping induces piezoelectric voltage generation and ferroelectric-photovoltaic effect. Adv Mater. 2015;27(28):4218–23. https://doi.org/10.1002/adma.201501594.
24. Ji W, Yao K, Liang YC. Bulk photovoltaic effect at visible wavelength in epitaxial ferroelectric $BiFeO_3$ thin films. Adv Mater. 2010;22(15):1763–6. https://doi.org/10.1002/adma.200902985.
25. Bai Z, Zhang Y, Guo H, Jiang A. The influence of conductive nanodomain walls on the photovoltaic effect of BiFeO3 thin films. Crystals. 2017;7(3):81. https://doi.org/10.3390/cryst7030081.
26. You L, et al. Enhancing ferroelectric photovoltaic effect by polar order engineering. Sci Adv. 2018. https://doi.org/10.1126/sciadv.aat3438.
27. He H, He Z, Jiang Z, Wang J, Liu T, Wang N. A controllable photoresponse and photovoltaic performance in Bi4Ti3O12 ferroelectric thin films. J Alloys Compd. 2017;694:998–1003. https://doi.org/10.1016/j.jallcom.2016.10.160.
28. Ehsani MH, Esmaeili S, Aghazadeh M, Kameli P, Tehrani FS, Karimzadeh I. An investigation on the impact of Al doping on the structural and magnetic properties of Fe3O4 nanoparticles. Appl Phys A Mater Sci Process. 2019;125(4):1–9. https://doi.org/10.1007/S00339-019-2572-2/FIGURES/9.
29. Trukhanov SV, et al. Magnetic and dipole moments in indium doped barium hexaferrites. J Magn Magn Mater. 2018;457:83–96. https://doi.org/10.1016/J.JMMM.2018.02.078.
30. Mohamed WS, et al. Effect of heavy Dy3+ doping on the magnetic, structural, morphological, and optical characteristics of CuDyxFe2-xO4 nanoparticles. Ceram Int. 2024;50(16):28505–21. https://doi.org/10.1016/J.CERAMINT.2024.05.160.
31. Mohamed WS, Alzaid M, Abdelbaky MSM, Amghouz Z, García-Granda S, Abu-Dief AM. Impact of Co2+ substitution on microstructure and magnetic properties of CoxZn1-xFe2O4 nanoparticles. Nanomaterials. 2019;9(11):1602. https://doi.org/10.3390/NANO9111602.
32. Mohamed WS, Hadia NMA, Al Bakheet B, Alzaid M, Abu-Dief AM. Impact of Cu2+ cations substitution on structural, morphological, optical and magnetic properties of Co1-xCuxFe2O4 nanoparticles synthesized by a facile hydrothermal approach. Solid State Sci. 2022. https://doi.org/10.1016/J.SOLIDSTATESCIENCES.2022.106841.
33. Trandafir EV, Ciocarlan R, Pui A, Hempelmann R, Caltun OF. Influence of precipitating agent concentration on nanoparticles size and magnetic properties of zinc ferrites. Rev Chim. 2020;71(2):10–4. https://doi.org/10.37358/RC.20.2.7878.
34. Manohar A, Reddy GR, Roy N, Hatshan MR, Kim KH. Multifaceted characterization of a Zn0.9Ca0.1Fe2O4/CeO2/NiFe2O4 nanocomposite electrode for battery-type supercapacitors. Ceram Int. 2024;50(3):4307–14. https://doi.org/10.1016/J.CERAMINT.2023.10.300.
35. Manohar A, et al. Tailored Zn1-xMg0.5CuxFe2O4 nanoparticles: optimizing magnetic hyperthermia for enhanced efficacy and investigating cytotoxicity in normal and cancer cell lines. Mater Chem Phys. 2024;316: 129050. https://doi.org/10.1016/J.MATCHEMPHYS.2024.129050.
36. Manohar A, Vijayakanth V, Mameda N, Sivajee Ganesh K. Revolutionizing nanoscience: exploring the multifaceted applications and cutting-edge advancements in spinel CaFe2O4 nanoparticles—a review. Inorg Chem Commun. 2024;161: 111999. https://doi.org/10.1016/J.INOCHE.2023.111999.
37. Chakraborty A, Bhattacharjee B, Ahmaruzzaman M. A sustainable pathway for the photodegradation of Rhodamine B dye using Mn-doped CaFe2O4 anchored on citrus fruit peel-derived biochar matrix. Inorg Chem Commun. 2025. https://doi.org/10.1016/J.INOCHE.2024.113444.
38. Manohar A, et al. Exploring NiFe2O4 nanoparticles: electrochemical analysis and evaluation of cytotoxic effects on normal human dermal fibroblasts (HDF) and mouse melanoma (B16–F10) cell lines. Colloids Surf A Physicochem Eng Asp. 2024;682: 132855. https://doi.org/10.1016/J.COLSURFA.2023.132855.
39. Zhang Y, et al. Research progress of NiFe2O4 electrode materials in supercapacitors: Preparation, modification, structural regulation, and future challenges. Coord Chem Rev. 2024. https://doi.org/10.1016/J.CCR.2024.216103.
40. Manohar A, et al. Structural, BET, ESR, magnetic, electrochemical and cytotoxicity study of CeO2/NiFe2O4 nanocomposites. J Alloys Compd. 2023;968: 172275. https://doi.org/10.1016/J.JALLCOM.2023.172275.

41. Manohar A, Vattikuti SVP, Manivasagan P, Jang ES, Abdelghani HTM, Kim KH. Synthesis and characterization of CeO2/MgFe2O4 nanocomposites for electrochemical study and their cytotoxicity in normal human dermal fibroblast (HDF) and human breast cancer (MDA-MB-231) cell lines. J Alloys Compd. 2023;968: 171932. https://doi.org/10.1016/J.JALLCOM.2023.171932.
42. Manohar A, et al. Comprehensive characterization of a Mn0.1Mg0.9Fe2O4/CeO2/MgFe2O4 nanocomposite for high-performance supercapacitor applications. Ceram Int. 2024;50(7):10436–45. https://doi.org/10.1016/J.CERAMINT.2023.12.356.
43. Gao Z, Jia Z, Zhang J, Feng A, Huang Z, Wu G. Tunable microwave absorbing property of LaxFeO3/C by introducing a–site cation deficiency. J Mater Sci: Mater Electron. 2019;30(14):13474–87. https://doi.org/10.1007/s10854-019-01715-0.
44. Hou T, et al. A review of metal oxide-related microwave absorbing materials from the dimension and morphology perspective. J Mater Sci. 2019;30(12):10961–84. https://doi.org/10.1007/s10854-019-01537-0.
45. Reddy BC, et al. Synthesis and characterization of Barium ferrite nano-particles for X-ray/gamma radiation shielding and display applications. Prog Nucl Energy. 2022;147: 104187. https://doi.org/10.1016/j.pnucene.2022.104187.
46. R. Peymanfar, M. Rahmanisaghieh, A. Ghaffari, and Y. Yassi, "Preparation and identification of BaFe2O4 nanoparticles by the sol–gel route and investigation of its microwave absorption characteristics at ku-band frequency using silicone rubber medium," in The 3rd International Electronic Conference on Materials Sciences, Basel Switzerland: MDPI, May 2018, p. 5234. https://doi.org/10.3390/ecms2018-05234.
47. Raghavendra M, Mahesh SS, Dhananjay P, Srikantaswamy S, Ravikumar HB. Microwave hydrothermal synthesis of BaFe2O4 nanoparticles and dielectric study of PiBMA/BaFe2O4 polymer nanodielectrics. Mater Sci Eng, B. 2023;297: 116767. https://doi.org/10.1016/j.mseb.2023.116767.
48. Hu SL, Liu J, Yu HY, Liu ZW. Synthesis and properties of barium ferrite nano-powders by chemical co-precipitation method. J Magn Magn Mater. 2019;473:79–84. https://doi.org/10.1016/j.jmmm.2018.10.044.
49. Javidan A, Ramezani M, Sobhani-Nasab A, Hosseinpour-Mashkani SM. Synthesis, characterization, and magnetic property of monoferrite BaFe2O4 nanoparticles with aid of a novel precursor. J Mater Sci. 2015;26(6):3813–8. https://doi.org/10.1007/s10854-015-2907-5.
50. Peymanfar R, Rahmanisaghieh M. Preparation of neat and capped $BaFe_2O_4$ nanoparticles and investigation of morphology, magnetic, and polarization effects on its microwave and optical performance. Mater Res Express. 2018;5(10): 105012. https://doi.org/10.1088/2053-1591/aadaac.
51. Dilip R, Jayaprakash R. Synthesis and characterization of BaFe2O4 nano-ferrites for gas sensor applications. Energy Ecol Environ. 2018;3(4):237–41. https://doi.org/10.1007/s40974-018-0093-z.
52. Li K, Gu H, Wei Q. A novel hydrothermal synthesis method for barium ferrite. China Particuol. 2004;2(1):41–3. https://doi.org/10.1016/S1672-2515(07)60019-0.
53. Alamdari S, Hemmati M, Tafreshi J, Ehsani MH. Erbium doped barium tungstate-chitosan nanocomposite: luminescent properties. Prog Phys Appl Mater. 2023;3(2):119–23. https://doi.org/10.22075/PPAM.2023.31808.1065.
54. Manohar A, Reddy GR, Hatshan MR, Goud JP, Kim KH. Structural and magnetic properties of Ca0.5Mg0.5Fe2O4/CeO2/NiFe2O4 nanocomposite for energy storage applications. Ceram Int. 2023;49(22):35392–8. https://doi.org/10.1016/J.CERAMINT.2023.08.214.
55. Manohar A, Vijayakanth V. Electrochemical energy storage and photoelectrochemical performance of Ni1-XZnXFe2O4 nanoparticles. Mater Sci Semicond Process. 2023. https://doi.org/10.1016/J.MSSP.2023.107338.
56. Nikmanesh H, Moradi M, Bordbar GH, Shams Alam R. Effect of multi dopant barium hexaferrite nanoparticles on the structural, magnetic, and X-Ku bands microwave absorption properties. J Alloys Compd. 2017;708:99–107. https://doi.org/10.1016/j.jallcom.2017.02.308.
57. Nairan A, Khan U, Naz S, Saeed M, Wu D, Gao J. Effect of barium doping on structural and magnetic properties of nickel ferrite. Solid State Sci. 2022;131: 106965. https://doi.org/10.1016/j.solidstatesciences.2022.106965.
58. Mubasher, et al. Barium doping effects on frequency-dependent dielectric properties of cobalt ferrite nanoparticles. Materials Innovations. 2022;02(02):36–46. https://doi.org/10.54738/MI.2022.2201.
59. Batoo KM, Ijaz MF, Imran A, Pandiaraj S. Plasmonic Au nanoparticles enhanced photovoltaic characteristics of perovskite BiFeO3 nanostructures. J Mater Sci: Mater Electron. 2024;35(2):159. https://doi.org/10.1007/s10854-023-11902-9.
60. Batoo KM, Ijaz MF, Imran A, Pandiaraj S. Piezo-plasmon phototronically enhanced direct solar-chemical translations from Au decorated perovskite BiFeO3 sea urchin-like 3D nanostructures. Surf Int. 2023;40: 103137. https://doi.org/10.1016/j.surfin.2023.103137.
61. Bhojanaa KB, Ramesh M, Pandikumar A. Complementary properties of silver nanoparticles on the photovoltaic performance of titania nanospheres based photoanode in dye-sensitized solar cells. Mater Res Bull. 2020;122: 110672. https://doi.org/10.1016/J.MATERRESBULL.2019.110672.
62. Ciesielski A, Czajkowski KM, Switlik D. Silver nanoparticles in organic photovoltaics: finite size effects and optimal concentration. Sol Energy. 2019;184:477–88. https://doi.org/10.1016/J.SOLENER.2019.04.015.
63. Batoo KM, Ijaz MF, Imran A, Pandiaraj S. Duple charge separation and plasmonically enriched DSSC and piezo-photocatalytic efficacy of Au anchored perovskite Gd3+:BiFeO3 nanospheres. Chemosphere. 2024;346: 140410. https://doi.org/10.1016/j.chemosphere.2023.140410.
64. Jasni AH, et al. Silver nanoparticles in various new applications. Silver Micro Nanopart Prop Synthesis Characteriz Appl. 2021. https://doi.org/10.5772/INTECHOPEN.96105.
65. Bouafia A, et al. The recent progress on silver nanoparticles: synthesis and electronic applications. Nanomaterials. 2021;11(9):2318. https://doi.org/10.3390/nano11092318.
66. Talabani RF, Hamad SM, Barzinjy AA, Demir U. Biosynthesis of silver nanoparticles and their applications in harvesting sunlight for solar thermal generation. Nanomaterials. 2021;11(9):2421. https://doi.org/10.3390/nano11092421.
67. Naeem Ashiq M, et al. Enhanced electrochemical properties of silver-coated zirconia nanoparticles for supercapacitor application. J Taibah Univ Sci. 2021;15(1):10–6. https://doi.org/10.1080/16583655.2020.1867338.
68. Mali A, Ataie A. Influence of the metal nitrates to citric acid molar ratio on the combustion process and phase constitution of barium hexaferrite particles prepared by sol–gel combustion method. Ceram Int. 2004;30(7):1979–83. https://doi.org/10.1016/j.ceramint.2003.12.178.
69. Azis RS, et al. Influence of pH adjustment parameter for Sol-Gel modification on structural, microstructure, and magnetic properties of nanocrystalline strontium ferrite. Nanoscale Res Lett. 2018;13(1):160. https://doi.org/10.1186/s11671-018-2562-x.

70. Babu A, et al. Effect of pH variation on citrate nitrate sol-gels obtained from auto-combustion method: synthesis, calculations and characterisations of extremely dense BaZrO3 ceramic. Open Ceramics. 2022;12: 100303. https://doi.org/10.1016/j.oceram.2022.100303.
71. Chang Q, Cerneaux S, Wang X, Zhang X, Wang Y, Zhou JE. Evidence of ZrO2 sol–gel transition by gelation time and viscosity. J Solgel Sci Technol. 2015;73(1):208–14. https://doi.org/10.1007/S10971-014-3516-0/FIGURES/6.
72. Sutka A, Mezinskis G. Sol-gel auto-combustion synthesis of spinel-type ferrite nanomaterials. Front Mater Sci. 2012;6(2):128–41. https://doi.org/10.1007/S11706-012-0167-3/METRICS.
73. Crystal Lattice Structures: Orthorhombic Space Groups. Accessed: Jan. 12, 2025. https://www.atomic-scale-physics.de/lattice/spcgrp/orthorhombic.html
74. Sivakumar A, et al. Assessment of shock resistance of barium ferrite at dynamic shocked conditions. J Mater Sci: Mater Electron. 2021;32(17):22429–39. https://doi.org/10.1007/S10854-021-06729-1/FIGURES/7.
75. Ganose AM, Jain A. Robocrystallographer: automated crystal structure text descriptions and analysis. MRS Commun. 2019;9(3):874–81. https://doi.org/10.1557/MRC.2019.94.
76. Saravani H, Esmaeilzaei MR, Ghahfarokhi MT. Synthesis and characterization of ferromagnetic BaFe2O4 nanocrystals using novel ionic precursor complex [Fe(opd)3]2[Ba(CN)8]. J Inorg Organomet Polym Mater. 2016;26(2):353–8. https://doi.org/10.1007/s10904-016-0327-5.
77. Dilip R, Jayaprakash R. Supremacy of magnetic behaviour in n-heptane based M doped barium ferrite (BaFe2O4) nanoparticles (M: Co, Ni and Mn). J Inorg Organomet Polym Mater. 2021;31(7):3154–63. https://doi.org/10.1007/s10904-021-01963-w.
78. Snee P, Jawaid A, Bragg diffraction from 2-D nanoparticle arrays adapted by.
79. Fultz B, Howe J, Transmission electron microscopy and diffractometry of materials, 2013, https://doi.org/10.1007/978-3-642-29761-8.
80. Hasan SGA, Gupta AV, Reddi BV. Estimation of size and lattice parameter of magnetic nanoparticles based on XRD synthesized using arc-discharge technique. Mater Today Proc. 2021;47:4137–41. https://doi.org/10.1016/J.MATPR.2021.08.146.
81. Prieur D, et al. Size dependence of lattice parameter and electronic structure in CeO 2 nanoparticles. Inorg Chem. 2023;19:20. https://doi.org/10.1021/acs.inorgchem.0c00506.
82. Monshi A, Foroughi MR, Monshi MR. Modified scherrer equation to estimate more accurately nano-crystallite size using XRD. World J Nano Sci Eng. 2012;02(03):154–60. https://doi.org/10.4236/wjnse.2012.23020.
83. Ashokkumar M, Muthusamy C. Role of ionic radii and electronegativity of co-dopants (Co, Ni and Cr) on properties of Cu doped ZnO and evaluation of In-vitro cytotoxicity. Surf Interfaces. 2022;30: 101968. https://doi.org/10.1016/J.SURFIN.2022.101968.
84. Khan MAM, Kumar S, Ahmed J, Ahamed M, Kumar A. Influence of silver doping on the structure, optical and photocatalytic properties of Ag-doped BaTiO3 ceramics. Mater Chem Phys. 2021;259: 124058. https://doi.org/10.1016/J.MATCHEMPHYS.2020.124058.
85. Kamila R, Kurniawan B. The effect of Ag-doping (x = 0 and 0.05) on structural and morphological La 0.8-x Ag x Ca 0.2 MnO 3 material synthesized by sol-gel method The effect of Ag-doping (x = 0 and 0.05) on structural and morphological La0.8-xAgxCa0.2MnO3 material synthesized by sol-gel method. IOP Conf Series. 2019. https://doi.org/10.1088/1757-899X/496/1/012019.
86. Cheema H, et al. Structural, optical and electrical properties of Mn-doped ZnFe2O4 synthesized using sol–gel method. J Mater Sci Mater Electron. 2021;32(18):23578–600. https://doi.org/10.1007/S10854-021-06847-W/TABLES/4.
87. Hodoroaba V-D, Motzkus C, Macé T, Vaslin-Reimann S. Performance of high-resolution SEM/EDX systems equipped with transmission mode (TSEM) for imaging and measurement of size and size distribution of spherical nanoparticles. Microsc Microanal. 2014;20(2):602–12. https://doi.org/10.1017/S1431927614000014.
88. Dilip R, et al. Enhancement of magnetic and dielectrics performance of BaFe2O4 nanoparticles influenced by tri-sodium citrate as surfactant. J Mater Sci Mater Electron. 2022;33(30):23841–50. https://doi.org/10.1007/S10854-022-09142-4.
89. R. Jeevan Kumar, U. Naresh, T. Ramaprasad, and M. Prakash, Structural Morphological Properties of BaFe 2 O 4 Nano-Particles, vol. 5, 2018, Accessed: Oct. 19, 2023. www.jetir.org
90. Zhang XF, Liu ZG, Shen W, Gurunathan S. Silver nanoparticles: synthesis, characterization, properties, applications, and therapeutic approaches. Int J Mol Sci. 2016. https://doi.org/10.3390/IJMS17091534.
91. Yang Z, Yang N, Pileni MP. Nano Kirkendall effect related to nanocrystallinity of metal nanocrystals: influence of the outward and inward atomic diffusion on the final nanoparticle structure. J Phys Chem C. 2015;119(39):22249–60.
92. Kharisov BI, Dias HVR, Kharissova OV. Mini-review: ferrite nanoparticles in the catalysis. Arab J Chem. 2019;12(7):1234–46. https://doi.org/10.1016/J.ARABJC.2014.10.049.
93. Kim KJ et al., Inter-laboratory comparison: quantitative surface analysis of thin Fe-Ni alloy films, https://doi.org/10.1002/sia.3795.
94. Lambert A, et al. Synthesis and characterization of bimetallic Fe/Mn oxides for chemical looping combustion. Energy Procedia. 2009;1(1):375–81. https://doi.org/10.1016/J.EGYPRO.2009.01.051.
95. Hodoroaba VD, Rades S, Salge T, Mielke J, Ortel E, Schmidt R. Characterisation of nanoparticles by means of high-resolution SEM/EDS in transmission mode. IOP Conf Ser Mater Sci Eng. 2016;109(1): 012006. https://doi.org/10.1088/1757-899X/109/1/012006.
96. Eluyemi MS, et al. Synthesis and characterization of graphene oxide and reduced graphene oxide thin films deposited by spray pyrolysis method. Graphene. 2016;5(3):143–54. https://doi.org/10.4236/GRAPHENE.2016.53012.
97. Syed B, Nagendra NP. Synthesis of silver nanoparticles by endosymbiont Pseudomonas fluorescens CA 417 and their bactericidal activity. Enzyme Microb Technol. 2016;95:128–36. https://doi.org/10.1016/J.ENZMICTEC.2016.10.004.
98. Singh H, Du J, Yi TH. Kinneretia THG-SQI4 mediated biosynthesis of silver nanoparticles and its antimicrobial efficacy. Artif Cells Nanomed Biotechnol. 2017;45(3):602–8. https://doi.org/10.3109/21691401.2016.1163718.
99. Hodoroaba VD. Energy-dispersive X-ray spectroscopy (EDS). Characteriz Nanopart Measure Proc Nanopart. 2020. https://doi.org/10.1016/B978-0-12-814182-3.00021-3.
100. Rupp A, Göser J, Li Z, Altpeter P, Bilgin I, Högele A. Energy dispersive X-ray spectroscopy of atomically thin semiconductors," Jan. 2022, Accessed: Dec. 23, 2024. https://arxiv.org/abs/2201.12545v2
101. Akhtar MN, Khan MA. Effect of rare earth doping on the structural and magnetic features of nanocrystalline spinel ferrites prepared via sol gel route. J Magn Magn Mater. 2018;460:268–77. https://doi.org/10.1016/J.JMMM.2018.03.069.
102. Samoila P, et al. Nanosized spinel ferrites synthesized by sol-gel autocombustion for optimized removal of azo dye from aqueous solution. J Nanomater. 2015. https://doi.org/10.1155/2015/713802.

103. Fang Y, Zhang S, Ohodnicki PR, Wang G. Relation between cation distribution and chemical bonds in spinel NiFe2O4. Mater Today Commun. 2022;33: 104436. https://doi.org/10.1016/J.MTCOMM.2022.104436.
104. Dilip R, Jayaprakash R. Requisite of surfactant (CTAB, n-heptane, and tri-sodium citrate) levels on enhancement of magnetic property and morphology changes of barium ferrite (BaFe2O4) nanoparticles. J Supercond Nov Magn. 2020;33(12):3799–808. https://doi.org/10.1007/S10948-020-05645-5.
105. Heiba ZK, Wahba AM, Mohamed MB. Phase analysis and cation distribution correlated with magnetic properties of spinel Ba1−xSrxFe2O4 ferrites prepared at different annealing temperatures. J Mater Sci Mater Electron. 2020;31(15):12482–92. https://doi.org/10.1007/S10854-020-03795-9.
106. Shen P, Luo J, Zuo Y, Yan Z, Zhang K. Effect of La-Ni substitution on structural, magnetic and microwave absorption properties of barium ferrite. Ceram Int. 2017;43(6):4846–51. https://doi.org/10.1016/J.CERAMINT.2016.12.107.
107. Hublikar LV, Ganachari SV, Patil VB. Zn and Co ferrite nanoparticles: towards the applications of sensing and adsorption studies. Environ Sci Pollut Res. 2023;30(25):66994–7007. https://doi.org/10.1007/S11356-023-27201-Z/FIGURES/9.
108. Khan IS, Gul IH. Comparative investigation of magnetic, di-electric, optical, and electrical properties of mono-BaFe2O4 and hexa-BaFe12O19 nano-ferrites for photovoltaic (PV) applications. Appl Phys A Mater Sci Process. 2022. https://doi.org/10.1007/S00339-022-06214-4.
109. Ahmad M, Grössinger R, Ali I, Ahmad I, Rana MU. Synthesis and characterization of Al-substituted W-type hexagonal ferrites for high frequency applications. J Alloys Compd. 2013;577:382–8. https://doi.org/10.1016/J.JALLCOM.2013.05.135.
110. Abdelghany AM, Meikhail MS, Abdelraheem GEA, Badr SI, Elsheshtawy N. Lepidium sativum natural seed plant extract in the structural and physical characteristics of polyvinyl alcohol. Int J Environ Stud. 2018;75(6):965–77. https://doi.org/10.1080/00207233.2018.1479564.
111. Jabbar WA, Habubi NF, Chiad SS. Optical characterization of silver doped poly (Vinyl Alcohol) Films," *J Ark Acad Sci*, vol. 64, no. 1, Jan. 2010, Accessed: Oct. 20, 2023. https://scholarworks.uark.edu/jaas/vol64/iss1/21
112. Restelli S, Albini B, Bonomi S, Bini M, Mozzati MC, Galinetto P. Raman study of the laser-induced decomposition of ZnFe2O4 nanoparticles. Mater Today Commun. 2023;35: 106405. https://doi.org/10.1016/J.MTCOMM.2023.106405.
113. (PDF) Crystallography Online: Bilbao crystallographic server. Accessed: Nov. 01, 2023. https://www.researchgate.net/publication/228841764_Crystallography_Online_Bilbao_Crystallographic_Server
114. Raman spectroscopy study, magnetic and microwave absorbing properties of modified barium strontium monoferrite Ba(1-x)Sr(x)Fe2O4 | Request PDF. Accessed: Nov. 01, 2023. https://www.researchgate.net/publication/323626970_Raman_spectroscopy_study_magnetic_and_microwave_absorbing_properties_of_modified_barium_strontium_monoferrite_Ba1-xSrxFe2O4
115. Andreasson J, et al. Franck-Condon higher order lattice excitations in the la Fe1-x Crx O3 (x=0, 0.1, 0.5, 0.9, 1.0) perovskites due to Fe-Cr charge transfer effects. Phys Rev B Condens Matter Mater Phys. 2007. https://doi.org/10.1103/PHYSREVB.75.104302.
116. Andreozzi GB, Bersani D, Paolo Lottici P. Raman fingerprint of chromate, aluminate and ferrite spinels synthetic and natural spinel single crystals having compositions closely approaching spinel end-members ZnCr. J Raman Spectrosc. 2015. https://doi.org/10.1002/jrs.4764.
117. Galinetto P, Albini B, Bini M, Mozzati MC. Raman spectroscopy in zinc ferrites nanoparticles. Raman Spectroscopy. 2018. https://doi.org/10.5772/INTECHOPEN.72864.
118. Wang M, et al. A preliminary study of oxides of Fe doped with Ba Co, Cu and synthetized by the citrate sol–gel combustion route. J Phys Conf Ser. 2020;1541(1): 012013. https://doi.org/10.1088/1742-6596/1541/1/012013.
119. Fantozzi E, Rama E, Calvio C, Albini B, Galinetto P, Bini M. Silver doped magnesium ferrite nanoparticles: physico-chemical characterization and antibacterial activity. Materials. 2021;14(11):2859. https://doi.org/10.3390/MA14112859/S1.
120. Kefeni KK, Msagati TAM, Nkambule TT, Mamba BB. Spinel ferrite nanoparticles and nanocomposites for biomedical applications and their toxicity. Mater Sci Eng C. 2020. https://doi.org/10.1016/J.MSEC.2019.110314.
121. Wesselinowa JM, Apostolova I. Size, anisotropy and doping effects on the coercive field of ferromagnetic nanoparticles. J Phys: Condens Matter. 2007;19(40): 406235. https://doi.org/10.1088/0953-8984/19/40/406235.
122. Khajonrit J, Wongpratat U, Kidkhunthod P, Pinitsoontorn S, Maensiri S. Effects of Co doping on magnetic and electrochemical properties of BiFeO 3 nanoparticles. J Mag Mag Mater. 2017. https://doi.org/10.1016/j.jmmm.2017.10.092.
123. Zahn D, Diegel M, Valitova A, Dellith J, Dutz S. Magnetic barium hexaferrite nanoparticles with tunable coercivity as potential magnetic heating agents. Nanomaterials. 2024;14(12):992. https://doi.org/10.3390/NANO14120992.
124. Choudhary BL, et al. Irreversible magnetic behavior with temperature variation of Ni0.5Co0.5Fe2O4 nanoparticles. J Magn Magn Mater. 2020;507: 166861. https://doi.org/10.1016/J.JMMM.2020.166861.
125. Al Dairy AR, Al-Hmoud LA, Khatatbeh HA, 2019, Magnetic and structural properties of barium hexaferrite nanoparticles doped with titanium. Symmetry. 2019; 11: 732.
126. Lisjak D, Ovtar S. The alignment of barium ferrite nanoparticles from their suspensions in electric and magnetic fields. J Phys Chem B. 2013;117(6):1644–50. https://doi.org/10.1021/JP305256T/SUPPL_FILE/JP305256T_SI_001.PDF.
127. Li ZW, Lin GQ, Chen L, Wu YP, Ong CK. Size effect on the static and dynamic magnetic properties of W -type barium ferrite composites: from microparticles to nanoparticles. J Appl Phys. 2005;98(9):94310. https://doi.org/10.1063/1.2128688/924633.
128. Kumar S, Supriya S, Pradhan LK, Pandey R, Kar M. Grain size effect on magnetic and dielectric properties of barium hexaferrite (BHF). Physica B Condens Matter. 2020;579: 411908. https://doi.org/10.1016/J.PHYSB.2019.411908.
129. Dho J, Lee EK, Park JY, Hur NH. Effects of the grain boundary on the coercivity of barium ferrite BaFe12O19. J Magn Magn Mater. 2005;285(1–2):164–8. https://doi.org/10.1016/J.JMMM.2004.07.033.
130. Heiba ZK, Mohamed MB, Wahba AM. Effect of Mo substitution on structural and magnetic properties of Zinc ferrite nanoparticles. J Mol Struct. 2016;1108:347–51. https://doi.org/10.1016/J.MOLSTRUC.2015.12.042.
131. Tahir W, et al. Impact of silver substitution on the structural, magnetic, optical, and antibacterial properties of cobalt ferrite. Sci Rep. 2023;13(1):1–23. https://doi.org/10.1038/s41598-023-41729-7.
132. Fakhry F, Shaheen E, El-Dosoky H, Meaz TM, Mubark M, El-Shater R. Elastic and magnetic characteristics of nano-spinel ferrite Co0.5MgxCu0.5−xFe2O4. Sci Rep. 2024;14(1):1–16. https://doi.org/10.1038/s41598-024-74484-4.

133. Anukool W, et al. Effects of aluminum substitution on the microstructure and magnetic properties of cobalt ferrites prepared by the co-precipitation precursor. Appl Phys A Mater Sci Process. 2022;128(8):1–10. https://doi.org/10.1007/S00339-022-05831-3/TABLES/3.
134. Jadhav VV, Shirsat SD, Tumberphale UB, Mane RS. Properties of ferrites. Spinel Ferrite Nanostruct Energy Storage Dev. 2020. https://doi.org/10.1016/B978-0-12-819237-5.00003-1.
135. Palla BJ, Shah DO, Garcia-Casillas P, Matutes-Aquino J. Preparation of nanoparticles of barium ferrite from precipitation in microemulsions. J Nanopart Res. 1999;1(2):215–21. https://doi.org/10.1023/A:1010004616528.
136. Shen W, et al. Effects of high pressure on the electrical resistivity and dielectric properties of nanocrystalline SnO 2. Sci Rep. 2018. https://doi.org/10.1038/s41598-018-22965-8.
137. Suresh S. Studies on the dielectric properties of CdS nanoparticles. Appl Nanosci. 2014;4(3):325–9. https://doi.org/10.1007/S13204-013-0209-X/FIGURES/5.
138. Abassi H, Kumar U, Timoumi A, Bouguila N, Amdouni N, Bouchriha H. Effect of frequency on activation energy and its role in producing piezoelectricity for Ruddlesden popper oxide Ba2SnO4. Mater Chem Phys. 2023;309: 128338. https://doi.org/10.1016/J.MATCHEMPHYS.2023.128338.
139. Mazen SA, Abu-Elsaad NI. Structural, magnetic and electrical properties of the lithium ferrite obtained by ball milling and heat treatment. Appl Nanosci. 2015;5(1):105–14. https://doi.org/10.1007/S13204-014-0297-2/FIGURES/13.
140. Heiba ZK, Mohamed MB, Wahba AM, Arda L. Magnetic and structural properties of nanocrystalline cobalt-substituted magnesium-manganese ferrite. J Supercond Nov Magn. 2015;28(8):2517–24. https://doi.org/10.1007/S10948-015-3069-7/FIGURES/8.
141. Rama Krishna K, Ravinder D, Vijaya Kumar K, Joshi US, Rana VA, Lincon A. Dielectric properties of Ni-Zn ferrites synthesized by citrate gel method. World J Cond Matter Phys. 2012;2:57–60. https://doi.org/10.4236/wjcmp.2012.22010.
142. Cheema H, Kumar S, Alvi PA, Choudhary BL, Kumar U. Synthesis and physical properties of nanopowder and electrical properties of bulk samples of ZnFe2-xNixO4 (x: 0, 0.05, 0.10). Adv Powder Technol. 2020;31(10):4241–52. https://doi.org/10.1016/J.APT.2020.09.001.
143. Abu-Samaha FSH, Ismail MIM. AC conductivity of nanoparticles CoxFe(1–x)Fe2O4 (x=0, 0.25 and 1) ferrites. Mater Sci Semicond Process. 2014;19(1):50–6. https://doi.org/10.1016/J.MSSP.2013.11.027.
144. Khan IS, Gul IH. Unlocking the power of Zn-substituted barium ferrite (BaFe2O4) nanoparticles for unprecedented magnetic, dielectric, and optical enhancement for photovoltaic devices. J Mater Sci. 2024;35(25):1–34. https://doi.org/10.1007/S10854-024-13409-3.
145. Norouzzadeh P, Golzan MM, Mabhouti K, Naderali R. Effect of Mn-substitution on impedance spectroscopy and magnetic properties of Al-doped ZnO nanoparticles. Nanotechnology. 2020;31(32): 325704. https://doi.org/10.1088/1361-6528/AB8A8B.
146. Chen J, Zhai Y, Yu Y, Luo J, Fan X. Spatial separation of photo-induced charge carriers in a Na3VO2B6O11 polar material and its enhanced photocatalytic activity. Appl Surf Sci. 2021;556: 149809. https://doi.org/10.1016/J.APSUSC.2021.149809.
147. Kolanoski H, Wermes N. Particle detectors: Fundamentals and applications. Particle Detectors. 2020. https://doi.org/10.1093/oso/9780198858362.001.0001.
148. Shahzadi K, et al. Impact of aluminum substitution on the structural and dielectric properties of Ni–Cu spinel ferrite nanoparticles synthesized via sol–gel route. Opt Quantum Electron. 2020;52(4):1–17. https://doi.org/10.1007/S11082-020-02304-W/FIGURES/13.
149. L. B. Kong, H. Huang, and S. Li, Fundamentals of Ferroelectric Materials, 2018.
150. Zhao D, et al. Depolarization of multidomain ferroelectric materials. Nat Commun. 2019;10(1):1–11. https://doi.org/10.1038/s41467-019-10530-4.
151. e Silva IR, Lipan O, Hartmann F, Höfling S, Lopez-Richard V. Unveiling ferroelectric-like behavior in leaky dielectrics: a microscopic model for polarization dynamics and hysteresis inversion, 2024, Accessed: Jan. 05, 2025. http://arxiv.org/abs/2410.16084
152. Rani K, et al. Quantitative investigation of polarization-dependent photocurrent in ferroelectric thin films titative investigation of polarization-dependent photocurrent in ferroelectric thin films quantitative investigation of polarization-dependent photocurrent in ferroelectric thin films. J Phys. 2021;1:67.
153. Sarkar K, Harsh H, Rahman Z, Kumar V. Enhancing the structural, optical, magnetic and ferroelectric properties of perovskite BiFeO3 through metal substitution. Chem Phys Impact. 2024;8: 100478. https://doi.org/10.1016/J.CHPHI.2024.100478.
154. Dang Y, Tao X, Recent progress of bulk photovoltaic effect in acentric single crystals and optoelectronic devices, 2022, https://doi.org/10.1016/j.matt.2022.06.011.
155. Heiba ZK, Mohamed MB, Wahba AM, Imam NG. Structural, optical, and electronic characterization of fe-doped alumina nanoparticles. J Electron Mater. 2018;47(1):711–20. https://doi.org/10.1007/S11664-017-5830-0/METRICS.
156. Heiba ZK, Farag NM, El-naggar AM, Plaisier JR, Aldhafiri AM, Mohamed MB. Influence of Cr and Fe doping on the structure, magnetic and optical properties of nano CuCo2O4. Ceram Int. 2021;47(6):7888–97. https://doi.org/10.1016/J.CERAMINT.2020.11.135.
157. Mehta SK, Kumar S, Chaudhary S, Bhasin KK. Supplementary material (ESI) for nanoscale supplementary data nucleation and growth of surfactant passivated CdS and HgS NPs: time dependent absorption and luminescence profiles. Nanoscale. 2009. https://doi.org/10.1039/B9NR00070D.
158. Determination of the band gap of semiconductor nanoparticles | McGraw-Hill Education - Access Engineering. Accessed: Oct. 22, 2023. https://www.accessengineeringlibrary.com/content/book/9781259007323/back-matter/appendix11
159. Singh M, Goyal M, Devlal K. Size and shape effects on the band gap of semiconductor compound nanomaterials. J Taibah Univ Sci. 2018;12(4):470–5. https://doi.org/10.1080/16583655.2018.1473946.
160. Mosiori CO, Njoroge WK, Ochoo LO. Optical analysis of Ag-NPs containing methyl ammonium lead tri-iodide thin films. Path of Science. 2017;3(9):2007–15. https://doi.org/10.22178/POS.26-10.
161. Heiba ZK, Mohamed MB. Structural phase analysis, optical and magnetic properties of nano Mn-doped LiFe5O8. Appl Phys A Mater Sci Process. 2018;124(12):1–10. https://doi.org/10.1007/S00339-018-2241-X/FIGURES/8.
162. Jaykhedkar N, Bystrický R, Sýkora M, Bučko T. Understanding the structure-band gap relationship in SrZrS 3 at elevated temperatures: a detailed NPT MD study. J Mater Chem C Mater. 2022;10(33):12032–42. https://doi.org/10.1039/D2TC02253B.
163. Martino E, et al. Structural phase transition and bandgap control through mechanical deformation in layered semiconductors 1T-ZrX2(X = S, Se). ACS Mater Lett. 2020;2(9):1115–20. https://doi.org/10.1021/ACSMATERIALSLETT.0C00252/SUPPL_FILE/TZ0C00252_SI_001.PDF.
164. "[54] 5.1. What are concentrating photovoltaics? | EME 812: utility solar power and concentration (psu.edu)."

165. Devi EC, Singh SD. Magnetic and photoluminescence properties of rare-earth substituted quaternary spinel ferrite nanoparticles. Ceram Int. 2023;49(5):8409–16. https://doi.org/10.1016/J.CERAMINT.2022.11.003.
166. Kharisov BI, Dias HR, Kharissova OV. Mini-review: ferrite nanoparticles in the catalysis, 2014, https://doi.org/10.1016/j.arabjc.2014.10.049.
167. Chen P, et al. A room temperature ferroelectric material with photoluminescence: (1,3-dicyclohexylimidazole)2MnCl4. Dalton Trans. 2023;52(27):9448–55. https://doi.org/10.1039/D3DT01260C.
168. Borkar H, Mishra S, Gangwar J, Haranath D, Kumar A. Electric field modulated photoluminescence in ferroelectric ceramics for photosensitive device applications. Mater Res Bull. 2022;152: 111831. https://doi.org/10.1016/j.materresbull.2022.111831.
169. Canu G, et al. Ferroelectric order driven Eu3+ photoluminescence in BaZrxTi1−xO3 perovskite. Sci Rep. 2019;9(1):6441. https://doi.org/10.1038/s41598-019-42897-1.
170. Zhang XL, Zhu JJ, Zhang JZ, Xu GS, Hu ZG, Chu JH. Photoluminescence study on polar nanoregions and structural variations in Pb(Mg_1/3Nb_2/3)O_3-PbTiO_3 single crystals. Opt Express. 2014;22(18):21903. https://doi.org/10.1364/OE.22.021903.
171. Hasabeldaim EHH, Swart HC, Kroon RE. Luminescence and stability of Tb doped CaF2 nanoparticles. RSC Adv. 2023;13(8):5353–66. https://doi.org/10.1039/D2RA07897J.
172. Heiba ZK, Mohamed MB, Imam NG. The reflection of Cr/Fe substitution on the structural, magnetic and photoluminescence features of Zn–Ni based ferrite. J Supercond Nov Magn. 2017;30(11):3123–8. https://doi.org/10.1007/S10948-017-4112-7/FIGURES/3.
173. Yadav V, Bhatnagar R, Kumar U. Innovative computational techniques for DSSCs using machine learning: a review. Discov Electron. 2024;1(1):1–8. https://doi.org/10.1007/S44291-024-00022-1.
174. Wahba AM, Mohamed MB, Imam NG. Correlating structural, magnetic, and luminescence properties with the cation distribution of Co0.5Zn0.5+xFe2–xO4 nanoferrite. J Magn Magn Mater. 2016;408:51–9. https://doi.org/10.1016/J.JMMM.2016.02.027.
175. "Solar Cell I-V characteristic and solar cell I-V Curve." Accessed: Jan. 05, 2025. https://www.alternative-energy-tutorials.com/photovoltaics/solar-cell-i-v-characteristic.html
176. Yadav V, Bhatnagar R, Kumar U. Enhancement in the electrocatalytic and optoelectronic performance of cost-effective counter electrode VO2 for dye-sensitized solar cell (DSSC). Adv Condensed Matter Phys. 2024;2024(1):6613380. https://doi.org/10.1155/2024/6613380.